UNIVERSITY OF OKLAHOMA

GRADUATE COLLEGE

REVISITING THE MECHANISMS OF CLAY DAMAGE

A THESIS

SUBMITTED TO THE GRADUATE FACULTY

in partial fulfillment of the requirements for the

Degree of

MASTER OF SCIENCE

By

FELIPE PEREZ
Norman, Oklahoma
2016

Downloaded from SHAREOK. Persistent Handle URL: https://hdl.handle.net/11244/34541

REVISITING THE MECHANISMS OF CLAY DAMAGE

A THESIS APPROVED FOR THE
MEWBOURNE SCHOOL OF PETROLEUM AND GEOLOGICAL
ENGINEERING

BY

Dr. Ahmad Jamili, Chair

Dr. Xingru Wu

Dr. Maysam Pournik

© Copyright by FELIPE PEREZ 2016
All Rights Reserved.

"Do you want to make God laugh? Tell Him your plans."

To my wife, Andrea. Together, we have made God laugh.

Acknowledgements

In the first place, I thank God, because *I can do all things through Christ who strengthens me* (Philippians 4:13).

I want to thank Dr. Ahmad Jamili for having given me the opportunity to come to The University of Oklahoma. He saw something in me that I was not aware I had, and for believing in me even when I did not believe in myself. His patience and guidance, especially in those moments when I was weak, always inspired me to continue.

I also want to thank Dr. Liangliang Huang for our countless meetings and for his help in figuring out why the simulations were not doing what they were supposed to do. He continually challenged me to devise new ideas and solutions. Ultimately, I think this is the most effective way to learn. His comments and critiques also helped form a better scientist.

My most sincere appreciation to Dr. Xingru Wu, who supported my ideas in bringing physics approaches to bear on issues in petroleum engineering. His assignments challenged me to find connections between physics engineering and petroleum engineering, with surprising results. Dr. Wu is also part of my committee, along with Dr. Maysam Pournik. I owe them both a debt of gratitude, for they encouraged me to do a great job.

All my gratitude and love to my family. My parents have always supported

me no matter the situation. For their good example, I am grateful. The person I have become is the result of their hard work over the years. To Juan, my brother, for showing me the path to follow. With every conversation, I learn something new. His wisdom and eloquence have guided me through difficult moments. To Jose, my youngest brother, for supporting what I love the most in my home country. I know he is not aware of this yet, but his sense of responsibility gives me peace in the distance and motivates me to continue. To Andrea's family, for being the ones who pushed me to pursue my dreams.

Last but not least, my journey through this exciting academic experience would not have been possible if I had not had some stability in my life. My heartiest gratitude to my wife, Andrea, for all her patience and support. To our heart friends Fr. Jim (and Fraiser), Edwin, Ed, Pat, Jay, Marie, Vickie, Pierce, Lori, Dan, Yoana, and Dr. Jean-Claude Roegiers and his wife Jeanne. Thank you for being the face of Christ to me during these last couple of years, and for years to come!

Table of Contents

Acknowledgements **iv**

List of Tables **viii**

List of Figures **ix**

Abstract **xi**

1 Introduction **1**

1.1 Formation damage and clay stability 2

1.2 Effects of clay damage in the oilfield 8

1.3 Research goal 9

1.4 Scope 9

2 Clay generalities **11**

2.1 Introduction 11

2.2 Phyllosilicates 12

2.3 Types of phyllosilicates 13

2.4 Pyrophyllite structure 14

2.5 Montmorillonite structure 17

3 Classical simulations **19**

3.1 Introduction 19
3.2 Force fields 20
3.2.1 The Born–Oppenheimer approximation 21
3.2.2 Force field implementations 23
3.3 Clayff force field 24

4 Simulations setup **29**
4.1 Montmorillonite models 29
4.2 Simulation parameters 31
4.3 Reservoir conditions 31

5 Results and discussion **33**
5.1 Introduction 33
5.2 Basal spacing 34
5.2.1 Na-montmorillonite 34
5.2.2 K-montmorillonite 35
5.3 Distribution of cations and water molecules in the interlayer region . 40
5.3.1 Na-montmorillonite 40
5.3.2 K-montmorillonite 41
5.4 Clay stability and damage 43

6 Conclusions and recommendations **50**
6.1 Conclusions 50
6.2 Recommendations 52

References **54**

List of Tables

2.1 Major groups of clay minerals 14

3.1 Nonbonded parameters for the Clayff force field 27

3.2 Bonded parameters for the Clayff force field 28

List of Figures

1.1 Swelling effect of the Na- and Ca-montmorillonites 5

1.2 Comparison between basal spacing of Na- and Ca-montmorillonites under hydration 6

1.3 Schematic explanation of the Reed (1977) mechanism for particle generation by mica alteration during exposure to low-potassium brine 8

2.1 Structural features of phyllosilicates 13

2.2 Dioctahedral structures 16

2.3 Na-montmorillonite substitutions 18

3.1 Representation of the variables used in functional forms by force fields 22

3.2 Inversion angle using an improper torsion angle 22

4.1 Schematic representation of the clay/water system 30

5.1 Illustration of basal spacing and interlayer region 34

5.2 Swelling behavior of montmorillonite clays upon hydration. Comparison of calculated and experimental results 36

5.3 Swelling behavior and density profiles for 0W, 1W, and 2W 37

5.4 Na-montmorillonite. Density profileand interlayer arrangement of cations and O_{water} atoms 38

5.5 K-montmorillonite. Density profileand interlayer arrangement of cations and O_{water} atoms 39
5.6 Radial distribution functions for cations, oxygen and hydrogen atoms 44
5.7 Snapshot of the Na-montmorillonite looking along the y-axis 47
5.8 Comparison between interlayer regions with 39 water molecules/4 unit cells 48
5.9 Snapshot of the K-montmorillonite looking along the y-axis 49

Abstract

Molecular dynamics simulations were used to investigate the underlying mechanisms of water interaction with Wyoming-type montmorillonites. The study focused on (1) the clay swelling process for different cations with the same charge (Na^+ and K^+), and (2) the stability of clay structures under insertion of water. Simulations show that the ionic radius of the cations and their hydration energies seem to be the critical factors that determine the distribution of cations and water molecules in the interlayer region. The differences in cation distribution are the microscopical explanation as to why saturation of smectites with K^+ cations retards clay damage, when compared to saturation with Na^+ cations.

Chapter 1

Introduction

The use of clays dates back to ancient times. Kaoline, a mixture of minerals generally containing kaolinite, quartz, mica, feldespar, illite, and montmorillonite dates back to the third century BCE in China. Architecture, industry, and agriculture have used clays for years. Production of sun-dried or fired bricks for building construction still follows the procedures developed several centuries ago, as do clay-based products, including tiles for walls and floors, ceramics, earthenware, and pipes for drainage. Currently, the number and complexity of applications for clay is rising. For example, nanoparticles such as carbon nanotubes, nanocarbon, nanoclays, and metal oxides are being used as fillers or additives in polymers to modify their performance. All this is possible because of the most interesting characteristics of clay, its ability to swell and to mold under contact with water, and to retain the given shape when dry.

As mentioned by Uddin (2008), the concept of using nanoparticle fillers came from the talk *There's plenty room at the bottom* given by Richard Feynman on December 29, 1959, at the Annual Meeting of The American Physical Society (California Institute of Technology, Pasadena, CA)[1]. At that time, nanotechnology was

[1]Available online: `http://calteches.library.caltech.edu/47/`. Accessed on March 4,

perceived as the design, characterization, production, and application of structures, devices, and systems by controlling the shape and size of material particles on a nanometer scale (Lauterwasser, 2005).

In petroleum engineering, clays have been considered one of the most important factors that cause formation damage (see for instance Ohen and Civan, 1993), hence the significance of understanding the underlying mechanisms of such damage. On the other hand, they are also important as additives in the design of current drilling muds (the major component of bentonite is montmorillonite) and the creation of new and improved drilling fluids (see for instance Anderson et al., 2010). The following section presents the conventional wisdom in water and clay interactions, especially the underlying mechanisms to explain clay damage and clay instability.

1.1 Formation damage and clay stability

According to Civan (2007), formation damage is a generic term referring to the impairment of the permeability of petroleum–bearing formations by various adverse processes. It may be caused by several factors, including physico-chemical, chemical, biological, hydrodynamic, and thermal interactions of porous formations, particles, and fluids, and the mechanical deformation of formation under stress and fluid shear. These processes are triggered during the drilling, production, workover, and hydraulic fracturing operations. In general, mineral matter and fine particles loosely attached to the pore surface are at equilibrium with the pore fluids. Any variation in chemical, thermodynamic, and stress states may break the equilibrium conditions, inducing particle detachment and precipitation formation. Once ions and particles are introduced into the fluid phases, they become mobile and can then

2016.

interact freely with all the other components of rocks and fluids in many intricate ways to create severe reservoir formation damage problems.

Amaefule et al. (1988) concentrated on experimental findings that enhanced understanding of some of the various agents that produce formation damage. Civan (2007) lists them as follows:

1. Invasion of foreign fluids, such as water and chemicals used for improved recovery, drilling mud invasion, and workover fluids;

2. Invasion of foreign particles and mobilization of indigenous particles such as sand, mud fines, bacteria, and debris;

3. Operation conditions such as well flow rates and wellbore pressures and temperatures;

4. Properties of the formation fluids and porous matrix.

Bishop (1997) identified seven formation damage mechanisms, summarized here as follows:

1. Fluid–fluid incompatibilities, for example emulsions generated between invading oil-based mud filtrate and formation water;

2. Rock–fluid incompatibilities, for example contact of potentially swelling smectite clay or deflocculatable kaolinite clay by non-equilibrium water based fluids with the potential to severely reduce near wellbore permeability;

3. Solids invasion, for example the invasion of weighting agents or drilled solids;

4. Phase trapping/blocking, for example, the invasion and entrapment of water-based fluids in the near wellbore region of a gas well;

5. Chemical adsorption/wettability alteration, for example, emulsifier adsorption changing the wettability and fluid flow characteristics of a formation;

6. Fines migration, for example the internal movement of fine particulates within a rock's pore structure resulting in the bridging and plugging of pore throats;

7. Biological activity, for example the introduction of bacterial agents into the formation during drilling and the subsequent generation of polysaccharide polymer slimes which reduce permeability.

Petroleum-bearing formations are made up of various mineral oxides such as SiO_2, Al_2O_3, FeO, Fe_2O_3, MgO, K_2O, CaO, P_2O_5, MnO, TiO_2, Na_2O, and other elements and ions such as S and Cl^-, which form the porous matrix, and various swelling and nonswelling clays, some of which exist as tightly packed and blended minerals within the rock matrix, and some others are located inside the pore space loosely attached to the pore surfaces (Bucke, Jr. and Mankin, 1971). The latter have a greater chemical and physico-chemical formation damage potential because of their direct exposure to the pore fluids. In fact, fines migration and the interactions of clay minerals with aqueous solutions are the primarily responsible for formation damage measured as permeability impairment (Ohen and Civan, 1993). If swellable clays are lining the pore throats, a small amount of expansion can also cause severe reductions in permeability (Bennion, 2002). Particularly, smectites have a quite large surface area of 700 m^2/g, which makes them highly water sensitive, thereby causing loss of microporosity and permeability. Moreover, swelling effects are not the only mechanism for formation damage due to clays. Alteration of their structure due to instability can ultimately lead to fines generation due to the breaking of the structures.

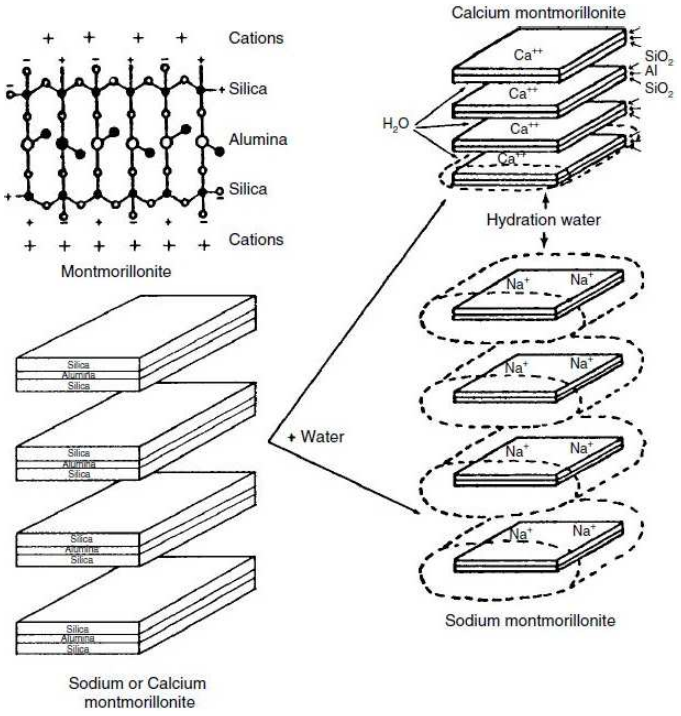


Figure 1.1: Swelling effect of the Na- and Ca-montmorillonites (taken from Civan (2007)).

The response of clays when in contact with water depends on the size, charge, and total amount of interlayer cations (Barshad, 1952). Formation damage due to clays must also depend on these parameters, as this research confirms. Mungan (1989) states that clay damage depends largely on (1) the type and amount of the exchangeable cations, and (2) the layered structure. Kaolinite is a nonswelling clay but will easily disperse and move. Montmorillonite (the most representative of the smectites) has a large base exchange capacity of 90 to 150 meq/100 g, and will readily adsorb Na^+, all leading to a high degree of swelling and dispersion. Illites combine the worst characteristics of the dispersible and the swellable clays, hence they are the most difficult to stabilize.

It is accepted that Na-montmorillonite swells more than Ca-montmorillonite because the Ca^{2+} cation is strongly adsorbed (by the clay surfaces) compared to the Na^+ cation (Gray and Darley, Gray and Darley). Accordingly, under con-

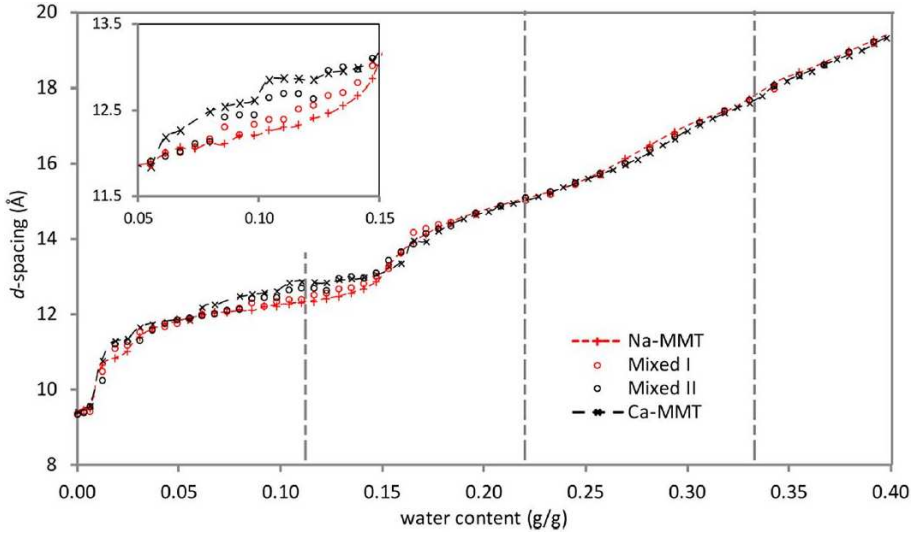


Figure 1.2: Comparison between basal spacing of Na- and Ca-montmorillonites under hydration (taken from Sun et al. (2015)). The legends correspond to different balancing positive charges origin: Na-mmt – only Na^+ cations; Mixed I – 2:1 ratio Na^+/Ca^{2+}; Mixed II – 1:2 ratio Na^+/Ca^{2+}; Ca-mmt – only Ca^{2+} cations.

tact with water, Ca-montmorillonine platelets remain practically intact and close to each other, whereas the Na-montmorillonite aggregates readily swell and the platelets separate widely. As a result, water can easily invade the gaps between the platelets and form thicker water envelopes around the Na-montmorillonite platelets than the Ca-montmorillonite platelets, as shown in Figure 1.1. However, recent studies using molecular dynamics simulations show that Na-montmorillonite and Ca-montmorillonite basal spacings are fairly similar if water content is less than 0.05 g H_2O/g clay or higher than 0.15 g H_2O/g clay, whereas for water content ranging between 0.05 and 0.15 g H_2O/g clay, Ca-montmorillonite exhibits stronger swelling than Na-montmorillonite (see Sun et al., 2015), as illustrated in Figure 1.2. Moreover, Ca^{2+} cations exhibit larger hydration energies relative to Na^+ cations, which leads to higher water coordination numbers and more pronounced association of water molecules with Ca^{2+} cations. These new results using molecular dynamics simulations demonstrate that the underlying mechanisms of clay swelling are still

open to discussion.

It is also accepted that clay damage can be prevented by maintaining high concentrations of K^+ cations in aqueous solutions. The proposed explanation is that due to the small size of the K^+ cation, it can readily penetrate the interlayers of the clay and hold the clay platelets together (Mondshine, 1973; Gray and Darley, Gray and Darley). To further support this statement, Reed (1977) conducted laboratory core tests by flowing deionized water, 3% NaCl brine, and 3% $CaCl_2$ brine through cores extracted from micaceous sand formations to determine permeability reduction, hypothesizing that mica alteration is a result of the exchange of K^+ cations with cations of larger sizes, such as Na^+, Li^+, Ca^{2+}, and Mg^{2+}, as depicted in Figure 1.3. Mica alteration generates fines that later deposit in porous rocks. When clays are exposed to low-salinity brines containing either no or small amounts of K^+ cations or larger cations, K^+ cations diffuse out of the clay platelets according to Fick's law due to the difference in concentrations between clay and brine, while larger cations diffuse into clays. Since larger cations cannot fit into the interlayer region, the edges of the friable mica flakes break off into small pieces. It is now known that the ionic radii[2] of the most common cations in clays are (in pm) Mg^{2+} (72) < Li^+ (76) < Ca^{2+} (100) < Na^+ (102) < K^+ (138) < Rb^+ (152) < Cs^+ (167) (Shannon, 1976), so that there must be an alternative mechanism that explains the generation of fines.

Carrying out a different experiment, Reed (1977) also noticed the dissolution by neutral salt solutions of significant amounts of carbonate present in natural carbonate cement, even though naturally occurring carbonate minerals have a low solubility. This phenomenon, along with mica alteration, free mineral particles that migrate with the flowing fluid, and ultimately can plug flow channels, reducing

[2]For a coordination of VI.

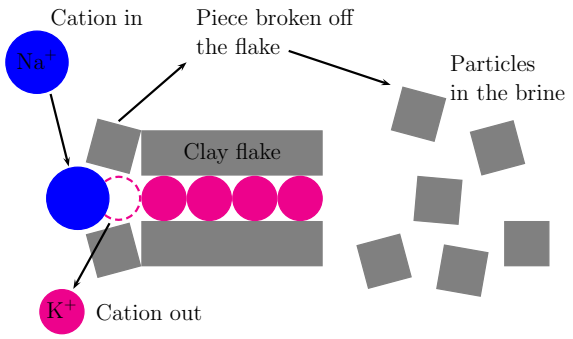


Figure 1.3: Schematic explanation of the Reed (1977) mechanism for particle generation by mica alteration during exposure to low-potassium brine (modified from Civan (2007)). Reed assumed that the ionic radius of Na^+ was larger than that of K^+.

permeability.

1.2 Effects of clay damage in the oilfield

Clay swelling and instability can have adverse impact on drilling operations and lead to significantly increased oil well construction costs. The drilling of oil and gas wells includes the use of fluids to lubricate the drill bit, maintain hydrostatic pressure, transmit sensor readings, remove rock cuttings, and inhibit swelling of reactive clay based shale formations. When water-based drilling fluids (WBDFs) are employed, clay damage can result in wellbore instability problems often identified by sloughing shales, hole closure causing tight hole, cave-ins leading to fill on trips and problems when running casing. Clay damage can also cause agglomeration of drilled cuttings leading to reduced rates of penetration arising from balling of the drill bit with sticky clay. In the worst case, wellbore instability can result in the loss of the drilling assembly, well side-tracks or total abandonment of the well (Anderson et al., 2010). All these problems can considerably decrease drilling rates and thus increase exploration and production costs. Several estimations for loss of production costs due to borehole instability problems agree that they can be easily greater than

$500 million per year (Bloys et al., 1994; Boek et al., 1995). Therefore, minimizing clay damage is an important area of study attracting a large amount of interest from both academia and industry. Understanding the mechanisms of clay swelling and instability to effectively reduce the extent of clay damage is then crucial for the development of efficient swelling clay inhibitors.

1.3 Research goal

The research goal is to provide alternate mechanisms that explain the effects of the interactions between water and clays. Clay swelling and the role that exchangeable cations play in their stability is of special interest. Molecular dynamics simulations have proven to be an excellent tool to run experiments that are difficult, if not impossible, to set up in laboratories while maintaining complete control as they are carried out. Here they are used to gain understanding on interactions between rocks (clays) and fluids (water).

1.4 Scope

This thesis has six chapters. Chapter 1 presents the conventional wisdom in water and clay interactions, specifically the underlying mechanisms explaining clay instability and damage. Chapter 2 describes some generalities of clays, a mineral group among the wider group of phyllosilicates, specifically the subgroup of smectites. The most representative smectite mineral is montmorillonite, the major component of bentonite clay minerals (that accounts for features such as low hydraulic conductivity, cation exchange, and swelling properties). Chapter 3 is a synopsis of a few ideas from the vast world of classical simulations. Chapter 4 describes how the simulations were set up. Chapter 5 presents the results obtained from the simu-

lations and discusses how they contrast with the conventional wisdom described in Chapter 1. Finally, Chapter 6 lists the conclusions and recommendations for future work.

Chapter 2

Clay generalities

2.1 Introduction

Broadly speaking, clays are a subset of minerals that may be described as hydrous silicates. Clays are naturally occurring materials formed by the weathering and decomposition of igneous rocks (McCabe, 1996) or other rocks, including shales (dark fine-grained sedimentary rocks composed of layers of compressed clay, silt, or mud). Examples of these processes are the chemical decomposition of granite that contains silica and alumina, the dissolution of limestone, and the disintegration and dissolution of shale.

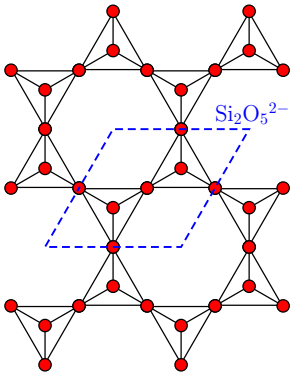
Clay minerals are materials based on two–dimensional stacks of inorganic layers (Boulet et al., 2006). The sheet–structured hydrous silicates are generally referred to as phyllosilicates, a wider group of minerals that includes micas, chlorite, serpentine, talc, and the so-called clay minerals (kaolinite, montmorillonite, illite). Clay minerals may be divided in four major groups, mainly based on the variation of the layered structure, as presented in Table 2.1. The kaolinite group has three polymorphic memebers (kaolinite, dickite, and nacrite) composed of silicate sheets

(SiO_5) bonded to aluminum oxide/hydroxide layers ($Al_2(OH)_4$). The smectite group is larger, having montmorillonite, talc, pyrophyllite, saponite, and nontronite among its members, whose differences are seen in their chemical characteristics. The illite group is represented by the mineral illite, the only common clay type. It is an important mineral in rock geochemistry and a main component of shales. The chlorite group is rather large and not necessarily considered as a part of the clay group, although it belongs to the phyllosilicates group.

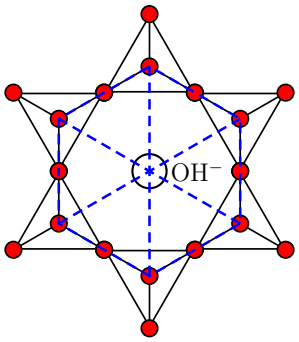
Smectites have non–equivalent substitutions of atoms that generate a negative charge on each layer surface, which is balanced by exchangeable interlayer cations. These cations are responsible for the differences in the physicochemical behavior of smectites such as water adsorption and retention, plasticity, and swelling, among others (Schoonheydt and Johnston, 2013). Thus, smectites are recognized as the most heterogeneous class of minerals with a pronounced variety in reactivity. Emmerich et al. (2009) revealed 96 possible structures in the montmorillonite-beidellite series of dioctahedral smectites, where several structures can occur simultaneously in a natural sample. In the particular case of swelling, smectite clay mineral particles consist of approximately one hundred layers into which additional molecules can be inserted, thereby changing the repetition distance along the layer normal (Bordallo et al., 2008; da Silva et al., 2002).

2.2 Phyllosilicates

Phyllosilicates are sheet silicates whose basic structure comprises interconnected six member rings of SiO_4^{4-} tetrahedrons. Three out of the four oxygen atoms from each tetrahedron are shared with other tetrahedrons; the basic structural unit is $Si_2O_5^{2-}$, as shown in Figure 2.1(a).



(a) Basic structural unit for phyllosilicates



(b) Hydroxyl cation centered among the six membered rings.

Figure 2.1: Structural features of phyllosilicates (modified from Nelson (2014)).

Most phyllosilicates contain an hydroxyl ion OH^- located at the center of the six membered rings, as shown in Figure 2.1(b). Thus, the basic structural unit becomes $Si_2O_5(OH)^{3-}$. When cations such as Fe^{2+}, Mg^{2+}, or Al^{3+}, are bonded to the SiO_4^{4-} sheets, they share the apical oxygen atoms and the OH^- ions, forming a layer of cations in octahedral coordination. The triangular faces of the tetrahedrons become the faces of the octahedral groups that can bind to the tetrahedral layers.

2.3 Types of phyllosilicates

Depending on the cation bonded to the SiO_4^{4-} sheet, the octahedral layers take on the structure of either brucite, $Mg(OH)_3$, if the cations have a charge +2, as Mg^{2+} or Fe^{2+}, or gibbsite, $Al(OH)_3$, if the cations have a charge +3 like Al^{3+}. All octahedral sites are occupied in brucite structure and all anions are OH^-, whereas in the gibbsite structure every third cation site is unoccupied and all anions are OH^- (Nelson, 2014). As a result, there are two types of sheet silicates:

- Trioctahedral, where each O or OH^- ion is surrounded by three divalent cations, like Mg^{2+} or Fe^{2+}; and

Table 2.1: Major groups of clay minerals (modified from Uddin (2008)).

Group name	Member minerals	General formula	Remarks
kaolinite	kaolinite, dickite, nacrite	$Al_2SiO_5(OH)_4$	Members are polymorphs (composed of the same formula and different structure).
montmorillonite/ smectite	montmorillonite, pyrophillite, talc, vermiculite, sauconite, saponite, nontronite	$(CaNa,H)(Al,Mg,Fe,Zn)_2$ $-(SiAl)_4O_{10}(OH)_2 \cdot nH_2O$	n indicates varying level of water in mineral type.
illite	illite	$(K,H)Al_2(Si,Al)_4O_{10}(OH)_2 \cdot nH_2O$	n indicates varying level of water in mineral type.
chlorite	(i) amesite (ii) chamosite (iii) cookeite (iv) nimite	(i) $(Mg,Fe)_4Al_4Si_2O_{10}(OH)_8$ (ii) $(Mg,Fe)_3Fe_3AlSi_3O_{10}(OH)_8$ (iii) $LiAl_5Si_3O_{10}(OH)_8$ (iv) $(Ni,Mg,Fe,Al)_6AlSi_3O_{10}(OH)_8$	Each member mineral has separate formula; this group has relatively larger member minerals and is sometimes considered as a separate group, not as part of clays.

- Dioctahedral, where each O or OH^- ion is surrounded by two trivalent cations, normally Al^{3+}.

2.4 Pyrophyllite structure

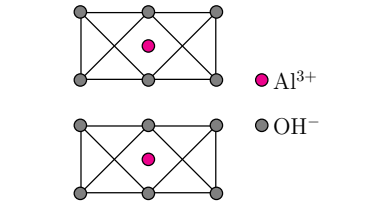
Pyrophyllite is one of the minerals that belongs to the smectite group and has a chemical formula $Al_2(Si_4O_{10})(OH)_2$. Its name comes from the Greek for *fire* ($\pi\tilde{\upsilon}\rho$, pyr) and *leaf* ($\phi\acute{\upsilon}\lambda\lambda o\nu$, phyllos) for the way it exfoliates when heated.

Pyrophyllite has a well-defined crystalline structure that has been been widely

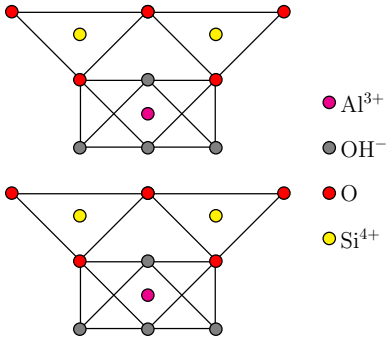
studied. It is possible to build the structure of pyrophyllite by starting with the octahedral layer of gibbsite (see Figure 2.2(a)), as explained by Nelson (2014). Replacing two of the OH^- ions with O, with O being the apical oxygen atoms of the tetrahedral sheets, the structure obtained corresponds to kaolinite (see Figure 2.2(b)). This leads to a tetrahedral–octahedral (T–O) structure, where each T–O layer is bonded to the top (or bottom) of another T–O layer by van der Waals interactions.

If two more of the OH^- ions on the octahedral layer are replaced by O, with O being the apical oxygen atoms of another tetrahedral layer, the structure obtained corresponds to pyrophyllite (see Figure 2.2(c)), and the whole structure is now a T–O–T layer that can be bonded to other T–O–T layers by means of weak van der Waals interactions.

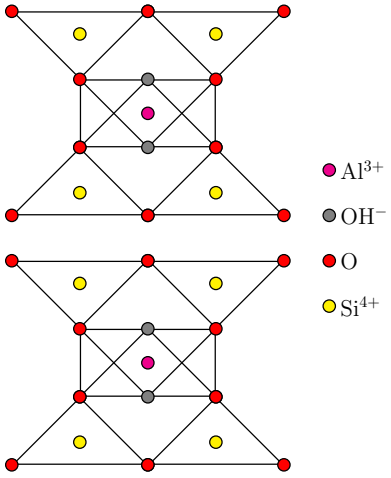
As mentioned previously, the crystalline properties of pyrophyllite have been widely studied and are well known. It can exist in three polytypic forms: a two layer monoclinic ($2M$), a one layer triclinic ($1Tc$), and a disordered form (Gruner, 1934; Zvyagin et al., 1969; Brindley and Wardle, 1970). Rayner and Brown (1964) came up with a monoclinic unit cell with parameters $a = 5.17$ Å, $b = 8.92$ Å, $c = 18.66$ Å, and $\beta = 99.8°$. From the absences in the diffraction pattern of pyrophyllite, they concluded that the space group was either $C2/c$ or Cc. Because of the additional systematic absences in its diffraction pattern, they also proposed that the structure was partially disordered, thereby there is a smaller monoclinic subcell with $a' = a = 5.17$ Å, $b' = b/3 = 2.97$ Å, $c' = c/2 = 9.33$ Å, $\beta' = \beta = 99.8°$, which belongs either to the space group Cm or $C2/m$. Brindley and Wardle (1970) used X–ray powder patterns of pyrophyllites from twenty localities to demonstrate that both one–layer triclinic and two–layer monoclinic forms exist, and from the best crystallized material they reported the unit cell parameters $a = 5.173$ Å, $b = 8.960$ Å, $c = 9.360$ Å, $\alpha = 91,2°$, $\beta = 100.4°$, and $\gamma = 90.0°$ for the $1Tc$ form, and $a = 5.172$



(a) Gibbsite structure



(b) Kaolinite structure



(c) Pyrophyllite structure

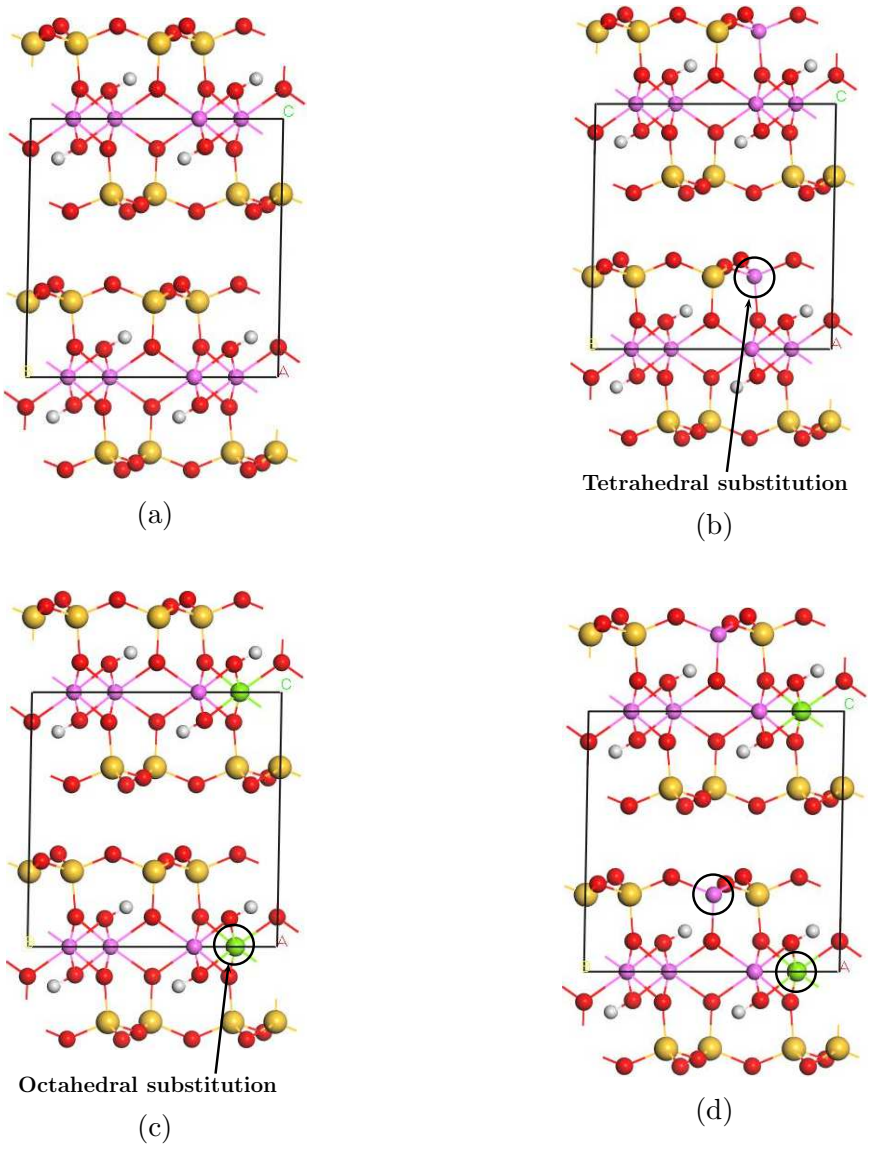
Figure 2.2: Dioctahedral structures

Å, $b = 8.958$ Å, $c = 18.67$ Å, and $\beta = 100.0°$ for the $2M$ form. Later, Wardle and Brindley (1972) determined the crystal structures of one–layer triclinic pyrophyllite and of its dehydroxylate by X–ray powder diffraction analysis. After least squares refinement of their previous results, the unit cell parameters for pyrophyllite $1Tc$ were reported to be $a = 5.161$ Å, $b = 8.957$ Å, $c = 9.351$ Å, $\alpha = 91,03°$, $\beta = 100.37°$, and $\gamma = 89.75°$. Lee and Guggenheim (1981) refined the crystal structure

of pyrophyllite from Ibitiara, Bahia, Brazil using least squares from single crystal X–ray data. This pyrophyllite crystal was found to be $1Tc$ polytype having space group of $C\overline{1}$ and unit cell parameters $a = 5.160$ Å, $b = 8.966$ Å, $c = 9.347$ Å, $\alpha = 91.18°$, $\beta = 100.46°$, and $\gamma = 89.64°$. The results presented by Lee and Guggenheim (1981) are in close agreement with the structural determination of Wardle and Brindley (1972). The Mineralogical Society of America accepts the parameters provided by Lee and Guggenheim (1981) in Anthony et al. (2001).

2.5 Montmorillonite structure

Montmorillonite is the most common mineral that belongs to the smectite group. In montmorillonites, each layer is composed of two tetrahedral silica sheets sandwiching one octahedral alumina sheet. Isomorphic substitution in the octahedral and/or tetrahedral layers creates a negative charge that is balanced by metal cations. Depending on the isomorphic substitution (tetrahedral, octahedral, or both), there are different kinds of montmorillonites (see Figure 2.3). The most studied montmorillonites have been the Wyoming–type that includes two types of substitution (tetrahedral and octahedral), for which the chemical composition of a unit cell is $(Si_{7.75}Al_{0.25})(Al_{3.5}Mg_{0.5})O_{20}(OH)_4$ and a negative charge of $-0.75e$ (e is the electronic charge), and Otay–type that includes only the octahedral substitution (Mignon et al., 2010).



(a) (b) (c) (d)

Figure 2.3: Na-montmorillonite substitutions. (a) Pyrophyllite (b) Tetrahedral substitution (c) Octahedral substitution (d) Double substitution. Balancing interlayer cations are not shown. Color code: yellow – silicon; red – oxygen; magenta – aluminum; green – magnesium; white – hydrogen.

Chapter 3

Classical simulations

3.1 Introduction

Accurate simulation of atomic and molecular systems involves the application of quantum mechanical theory, although currently its techniques are computationally expensive and are usually applicable only to small systems containing a few tens of atoms or small molecules. However, even if these simulations were possible, in most cases much of the information generated would be discarded because the goal when simulating large systems is often to extract bulk (statistical) properties that depend on the location of the atomic nuclei or, more realistically, an average over a set of atomic nuclei configurations. Consequently, the details of electronic motion are not of special interest and are lost in the averaging process. For this reason, semiclassical and classical simulations are now widely used, each employed depending on the nature of the problem. To investigate molecular systems, molecular dynamics (MD) simulations have proven to be a powerful tool. Bulk properties can be inferred if:

- A good approximation of the potential in which the atomic nuclei move is

available (the so-called force field); and

- There are methods that can generate a set of system configurations that are statistically consistent with a full quantum mechanical description (by using algorithms to integrate the classical Newton's equation of motion).

3.2 Force fields

In classical simulations, a force field describes an approximation of the potential energy hypersurface on which the atomic nuclei move. Force fields are usually tuned for particular groups of systems, hence the choice of a force field will depend on the type of structure under consideration.

In order to completely describe a molecule, it is necessary to make use of relativistic quantum theory, which is extremely complex due to the small scales and large velocities involved. A way to overcome this issue is to use MD simulations, classical simulations that integrate Newton's equations of motion and are based on empirical data that implicitly incorporate the relativistic and quantum effects (by means of force fields).

In non–relativistic quantum mechanics, the time–independent Schrödinger equation is (see for example Landau and Lifshitz, 1977)

$$\mathcal{H}\Psi(\mathbf{r},\mathbf{x}) = E\Psi(\mathbf{r},\mathbf{x}), \tag{3.1}$$

where $\mathcal{H}$ is the Hamiltonian of the system, Ψ is the wavefunction, and E is the energy. In general, Ψ is a function of the coordinates of the nuclei $\mathbf{r} \equiv \{\mathbf{r_1}, \mathbf{r_2}, \ldots, \mathbf{r_N}\}$ and of the electrons $\mathbf{x} \equiv \{\mathbf{x_1}, \mathbf{x_2}, \ldots, \mathbf{x_N}\}$.

3.2.1 The Born–Oppenheimer approximation

With the aim of solving the time–independent equation of Schrödinger, Eq.(3.1), some approximations are necessary. Born and Oppenheimer (1927) noticed that electrons are several thousands of times lighter than nuclei and move much faster, so that they decoupled the motion of electrons from that of the nuclei, giving two separate equations. The first of these equations describes the electronic motion[1],

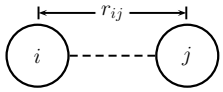
$$\mathcal{H}\Psi(\mathbf{x};\mathbf{r}) = E(\mathbf{r})\Psi(\mathbf{x};\mathbf{r}), \tag{3.2}$$

which depends parametrically on the positions of the nuclei $\mathbf{r}$, and $E(\mathbf{r})$ is usually called the potential energy surface. The second equation describes the motion of the nuclei on such a potential energy surface

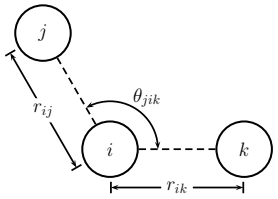
$$\mathcal{H}\Phi(\mathbf{r}) = E(\mathbf{r})\Phi(\mathbf{r}). \tag{3.3}$$

Solving Eq.(3.3) is important if the main interest is the structure or time evolution of a model. In principle, Eq.(3.2) could be solved for the potential energy $E(\mathbf{r})$ (it is customary to assume that the nuclei locations are fixed, and the fast movement of the electrons yields an electronic distribution and an average potential energy), and then Eq.(3.3) could be solved (the nuclei locations are released, allowing them to move under the effect of the average potential energy, leading to molecular vibrations and rotations)[2] (see for example Bransden and Joachain, 1983; Campos, Campos). This is, however, impractical due to the enormous effort required to solve Eq.(3.2). Instead, empirical fit to the potential energy surface (force field U) is used. Moreover, since the nuclei are heavy objects in the system, quantum

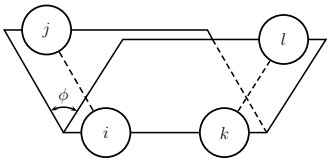
[1]The direct solution of Eq.(3.2) is the so–called *ab initio* calculation.
[2]This is called *adiabatic approximation* in molecular physics.



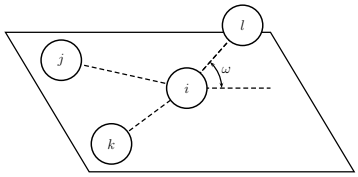
(a) Distance between two particles.



(b) Angle formed by three particles.



(c) Torsion angle formed by four particles.



(d) Inversion angle formed by four particles.

Figure 3.1: Representation of the variables used in functional forms by force fields (modified from Accelyrs, Inc. (2014)).

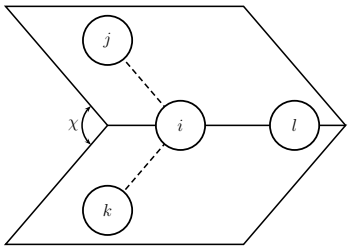


Figure 3.2: Inversion angle using an improper torsion angle (modified from Accelyrs, Inc. (2014)).

mechanical effects are often insignificant, and Eq.(3.3) can be replaced by Newton's equation of motion

$$-\nabla_{\mathbf{r}} U = m\frac{d^2\mathbf{r}}{dt^2}. \tag{3.4}$$

The solution of Eq.(3.4) (using an empirical fit to the potential energy surface $E(\mathbf{r})$) is called *molecular dynamics*.

3.2.2 Force field implementations

The purpose of a force field is to describe the potential energy hypersurface of entire classes of molecules with reasonable accuracy. The functional forms used in force fields employ a combination of internal coordinates and terms (bond distances, bond angles, dihedral angles, and inversion angles[3], as shown in Figure 3.1) to describe that part of the potential energy hypersurface due to interactions between atoms, and non–bond terms to describe the van der Waals (vdW), electrostatic (Coulomb), and hydrogen bond interactions between atoms. The functional forms range from simple quadratic forms to Morse functions, Fourier expansions, Lennard–Jones potentials, among others.

Some applications are beyond the capabilities of force fields, such as:

- Electron transitions (photon absorption);
- Electron transport phenomena; and
- Proton transfer (acid/base reactions).

On the other hand, the advantages of using force fields are:

- Force field–based calculations can handle large systems, because these calculation are several orders of magnitude faster and cheaper than quantum–based calculations;
- The energy can be broken up into different contributions, at the level of individual types of interactions; and
- The energy expression can be modified to impose further constrains.

[3]Some inversions use an improper torsion value, where the inversion angle χ is the angle between the jil and kil planes in Figure 3.2.

The force field type gives an indication of the nature and properties of a given particle in a simulation. If the simulation is atomistic, the principal determinant of the force field type is the element to which the atom belongs. In addition, the force field type also gives an indication of the nature of the local environment of a given atom. For example, an oxygen atom in water has a different local environment from that of one in carbon dioxide. The properties used to define a force field type might include a combination of:

- Element (if the particle is an atom);
- Type of bonds (single, double, triple, resonant, etc.);
- Number of particles to which the given particle is bonded;
- Type of particles to which the given particle is bonded;
- Hybridization; and
- Formal charge.

3.3 Clayff force field

Clayff is a force field first introduced by Cygan et al. (2004). It is based on the single point charge (SPC) water model of Berendsen et al. (1981) to represent water, hydroxyl, and oxygen–oxygen interactions. The SPC model has partial charges centered directly on each of three atoms, and the short–range interactions are represented by a Lennard–Jones (LJ) 12-6 term. Bond stretch and bond angle terms are introduced into the SPC model using the expressions determined by Teleman et al. (1987) to ensure full flexibility for the water and hydroxide components.

The total energy has contributions from the electrostatic interactions, the short–range interactions (represented by the van der Waals term), and bonded interactions, which in turn include bond stretch and angle bend, represented in the SPC model as harmonic terms. So, the total energy is expressed as

$$E_{\text{total}} = E_{\text{Coulomb}} + E_{\text{vdW}} + E_{\text{bond strecth}} + E_{\text{angle bend}}. \tag{3.5}$$

Coulombic and van der Waals interactions are excluded for intramolecular bonded interactions (i.e., 1–2 and 1–3 atom position exclusions); only intermolecular O–O and O–H nonbonded interactions (Coulombic and van der Waals terms) need to be evaluated in this case.

The Coulombic interaction is given by

$$E_{\text{Coulomb}} = \frac{e^2}{4\pi\epsilon_0} \sum_{i<j} \frac{q_i q_j}{r_{ij}^2}, \tag{3.6}$$

where the partial charges q_i and q_j are derived from quantum mechanics calculations, e is the charge of the electron, and ϵ_0 is the permitivity of free space. The van der Waals term, represented by the Lennard–Jones 12-6 function

$$E_{\text{vdW}} = \sum_{i<j} D_{0,ij} \left[\left(\frac{R_{0,ij}}{r_{ij}} \right)^{12} - 2 \left(\frac{R_{0,ij}}{r_{ij}} \right)^{6} \right], \tag{3.7}$$

includes the repulsive short–range (r^{-12}) term and the attractive long–range (r^{-6}) term. D_0 represents the depth of the potential well and R_0 is the distance at which the potential reaches its minimum value. The interaction parameters between unlike atoms are calculated according to the arithmetic mean rule for the distance parameter $R_{0,ij}$, and the geometric mean rule for the energy parameter $D_{0,ij}$, so that

$$R_{0,ij} = \frac{1}{2}(R_{0,i} + R_{0,j}), \tag{3.8a}$$

$$D_{0,ij} = \sqrt{D_{0,i} D_{0,j}}. \tag{3.8b}$$

The interactions associated with the hydrated phases metal–oxygen are considered ionic, allowing more flexibility in simulating complex and ill–defined crystal structures containing a large number of atoms and decreasing the risk of overparametrization by reducing the number of analytical expressions and force field parameters required to describe the energy of the atomic interactions throughout molecular dynamics simulations. The empirical parameters were optimized using the structures of simple oxides, hydroxydes, and oxyhydroxides, whereas the partial charges were derived from periodic density functional theory calculations of these compounds.

For phases containing hydroxyl groups, the bond stretch energy is described by a simple harmonic term as

$$E_{\text{bond stretch},ij} = k_1(r_{ij} - r_0)^2, \tag{3.9}$$

where k_1 represents the force constant and r_0 is the equilibrium bond length. The bonded hydrogen associated with the hydroxyl group does not require any nonbonded LJ component; only Coulombic interactions between hydrogen charges are required. Due to the inclusion of bonded terms between oxygen and hydrogen, intramolecular nonbonded interactions for them are excluded.

To better describe metal sorption on hydrated surfaces, and to improve the vibrational behavior of hydroxyl groups, an angle bend (three–body) term is included.

Table 3.1: Nonbonded parameters for the Clayff force field.

Species	Symbol	Charge [e]	D_0 [kcal/mol]	R_0 [Å]
water hydrogen	h*	0.4100		
hydroxyl hydrogen	ho	0.4250		
water oxygen	o*	−0.8200	0.1554	3.5532
hydroxyl oxygen	oh	−0.9500	0.1554	3.5532
bridging oxygen	ob	−1.0500	0.1554	3.5532
bridging oxygen with octahedral substitution	obos	−1.1808	0.1554	3.5532
bridging oxygen with tetrahedral substitution	obts	−1.1688	0.1554	3.5532
bridging oxygen with double substitution	obss	−1.2996	0.1554	3.5532
hydroxyl oxygen with substitution	ohs	−1.0808	0.1554	3.5532
tetrahedral silicon	st	2.1000	1.8405×10^{-6}	3.7064
octahedral aluminum	ao	1.5750	1.3298×10^{-6}	4.7943
tetrahedral aluminum	at	1.5750	1.8405×10^{-6}	3.7064
octahedral magnesium	mgo	1.3600	9.0298×10^{-7}	5.9090
hydroxide magnesium	mgh	1.0500	9.0298×10^{-7}	5.9090
octahedral calcium	cao	1.3600	5.0298×10^{-6}	6.2484
hydroxide calcium	cah	1.0500	5.0298×10^{-6}	6.2428
octahedral iron	feo	1.5750	9.0298×10^{-6}	5.5070
octahedral lithium	lio	0.5250	9.0298×10^{-6}	4.7257
aqueous sodium ion	Na	1.0000	0.1301	2.6378
aqueous potassium ion	K	1.0000	0.1000	3.7423
aqueous cesium ion	Cs	1.0000	0.1000	4.3002
aqueous calcium ion	Ca	2.0000	0.1000	3.2237
aqueous barium ion	Ba	2.0000	0.0470	4.2840
aqueous chloride ion	Cl	−1.0000	0.1001	4.9388

The energy of the angle bend is given by a simple harmonic term as

$$E_{\text{angle bend},ijk} = k_2(\theta_{ijk} - \theta_0)^2, \tag{3.10}$$

where k_2 represents the force constant and θ_0 is the equilibrium bond angle.

The nonbonded interaction parameters for Clayff are provided in Table 3.1. The Clayff bonded parameters for water and hydroxyl interactions are listed in Table 3.2.

Table 3.2: Bonded parameters for the Clayff force field.

Bond stretch			
Species i	Species j	k_1[kcal/mol·Å^2]	r_0[Å]
o*	h*	554.1349	1.0000
oh	ho	554.1349	1.0000
ohs	ho	554.1349	1.0000

Angle bend				
Species i	Species j	Species k	k_2[kcal/mol]	θ_0[deg]
h*	o*	h*	45.7696	109.47
Metal	oh	ho	30.00	109.47
Metal	ohs	ho	30.00	109.47

Chapter 4

Simulations setup

4.1 Montmorillonite models

This thesis considered a model of Wyoming–type montmorillonite with octahedral and tetrahedral substitutions, as schematically shown in Figure 4.1. The octahedral substitutions are such that two non-consecutive[1] Al^{3+} atoms are replaced with Mg^{2+}, and the tetrahedral substitution is such that one Si^{4+} is replaced with one Al^{3+}. The position of the tetrahedral substitution is not linked to any of the octahedral substitutions by an oxygen atom. Due to the isomorphic substitutions, no structural data with explicit location of substitutions is available in X–ray crystallographic databases. A common way to build up a model cell for montmorillonite is to start with the unit cell of pyrophyllite (Figure 2.3(a)), which has identical aluminosilicate layers to montmorillonite but exhibits no substitutions (see, for instance, Mignon et al. (2010)). Another way is to start with the atomic positions determined experimentally by Tsipursky and Drits (1984) for a smectite sample (see, for example, Minisini and Tsobnang (2005)). This thesis followed the first approach.

Two supercells were created, one composed of four unit cells ($4 \times 1 \times 1$ –

[1]The atoms are connected by neither one hydroxyl group nor an oxygen atom.

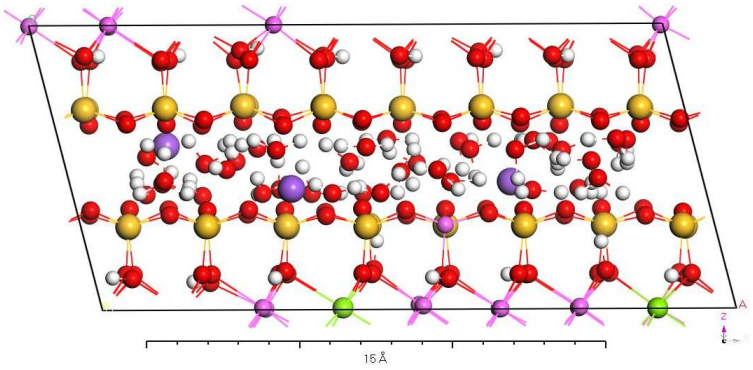


Figure 4.1: Schematic representation of the clay/water system. Notice the location of the tetrahedral and octahedral substitutions. Color code: yellow – silicon; red – oxygen; magenta – aluminum; green – magnesium; white – hydrogen; blue – sodium.

utilized for testing purposes) and the other one of sixty four unit cells ($8 \times 4 \times 2$), having a composition of $Na_3(Si_{31}Al)(Al_{14}Mg_2)O_{80}(OH)_{16} \cdot nH_2O$, where n varies from 0 to 15 water molecules/unit cell. Figure 4.1 shows a schematic representation of the montmorillonite layers and interlayer species (H_2O and Na^+). The unit cell of pyrophyllite is triclinic (belongs to space group $C\overline{1}$) with parameters $a = 5.160$ Å, $b = 8.966$ Å, $c = 9.347$ Å, $\alpha = 91.18°$, $\beta = 100.46°$, and $\gamma = 89.64°$, as reported by Lee and Guggenheim (1981).

The pyrophyllite structure was built using Materials Studio (Accelyrs, Inc., 2014); then Na^+ and K^+ cations were placed randomly in the region between the clay layers and the geometries were optimized individually using GULP (Gale and Rohl, 2003). Starting with these optimized structures, three water molecules per four unit cells were introduced into the simulation cell for each simulation, using Packmol (Martínez et al., 2009), up to a maximum of 60 water molecules/4 unit cell.

4.2 Simulation parameters

The MD simulations in this work were carried out using the Large–scale Atomic/ Molecular Massively Parallel Simulator, LAMMPS (Plimpton, 1995). VMD software was used for visualization purposes (Humphrey et al., 1996). Clayff force field was used to describe the interactions between atoms (Cygan et al., 2004, 2012). The Lorentz–Berthelot mixing rule was used to obtain the Lennard–Jones parameters for interactions between unlike atoms (Allen and Tildesley, 1989; Halgren, 1992), see Equations (3.8). The simulations were performed under periodic boundary conditions, with the long–range electrostatic term treated by the standard Ewald method (Allen and Tildesley, 1989). After running some tests with the smaller supercells, it was determined that an optimum cutoff distance for the nonbonded van der Waals interactions and for the Ewald summation of the electrostatic interactions was 15 Å. All simulations were carried out using an isobaric–isothermal (NpT) ensemble at $T = 300$ K and $p = 1$ atm. Pressure was controlled by the Parrinello–Rahman barostat (Parrinello and Rahman, 1981) while temperature was controlled by the Nosé–Hoover thermostat (Nosé, 1984a,b, 1991). The relaxation time for representative stages of no water layer (0W), one water layer (1W), and two water layers (2W) was 10 ns; for other stages it was 1 ns.

4.3 Reservoir conditions

Pressure and temperature were kept as low as $T = 300$ K and $p = 1$ atm instead of raising them to reservoir conditions, say $T = 348.15$ K and $p = 130$ bar, because Myshakin et al. (2013) demonstrated that the difference between these two conditions in the basal spacing is only slight[2]. It turns out that the basal spacing

[2]See Figure 2 in the work referenced.

is relatively insensitive to changes in pressure and temperature, with the degree of water content being the main factor controlling the extent of swelling. This is consistent with X-ray diffraction measurements of d-spacings showing that hydrate states are relatively stable with pressure (Fu et al., 1990; Giesting et al., 2012; Ilton et al., 2012). The results obtained at $T = 300$ K and $p = 1$ atm provide insights accurate enough for all intents and purposes.

Chapter 5

Results and discussion

5.1 Introduction

The concepts of basal spacing and interlayer region are illustrated in Figure 5.1. Barshad (1952) studied the factors affecting the interlayer expansion of vermiculite and montmorillonite with organic substances, and determined that the extent of interlayer expansion was affected primarily by the size, charge, and total amount of the cations and by the magnitude of the dipole moment and the dielectric constant of the immersion liquid. Norrish (1954) carried out experiments focused on the swelling of montmorillonite and confirmed that this effect exhibits two regimes: crystalline swelling and osmotic swelling. In crystalline swelling, adsorbed water increases to approximately 0.5 g H_2O/g clay while the interlayer spacing increases from 9.5 Å (for dry material) to ∼20 Å. Several other studies have shown that the swelling process occurs by increasing the water content through the formation of one, two, and perhaps three layer hydrates[1] (see for example Boek et al., 1995; Chou Chang et al., 1995; Cygan et al., 2004; Zheng et al., 2011). Osmotic swelling occurs when

[1]Sun et al. (2015) summarize several works in which the majority of experimental studies reported the formation of one-layer and two-layer hydrates, whereas the formation of the three-layer hydrate was observed only in a few studies. See the work referenced for further information.

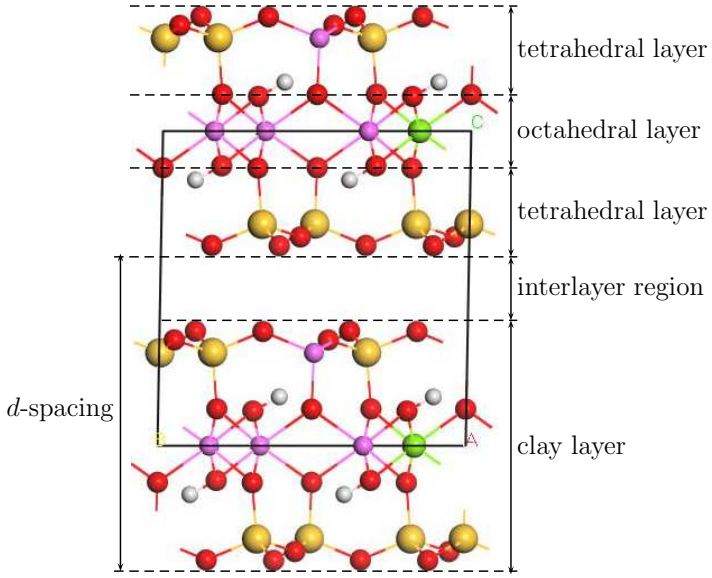


Figure 5.1: Illustration of basal spacing and interlayer region.

montmorillonite is placed in contact with water and takes up 10 g H_2O/g clay, increasing its volume by about twenty times.

5.2 Basal spacing

5.2.1 Na-montmorillonite

The basal spacing for Na-montmorillonite after hydration obtained from the simulations is presented in Figure 5.2(a) along with the experimental data obtained by Fu et al. (1990). The error bars represent two standard deviations. The simulation results are consistent with the experiment.

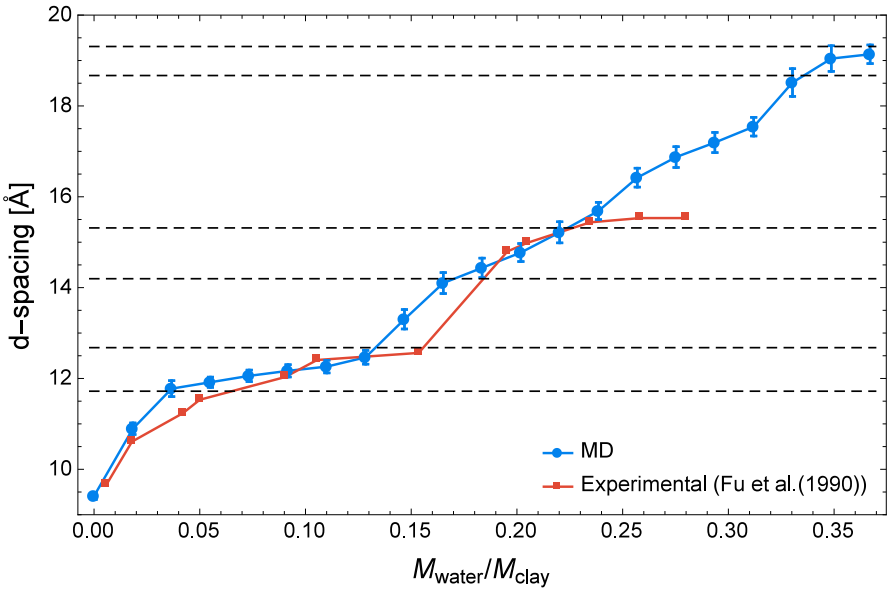
The results exhibit the expansion of the clay through two well–defined expanded layer structures (perhaps three layer structures if the incipient plateau in the region between 18.7 Å and 19.3 Å is also considered), displaying plateaus corresponding to formation of monolayer and bilayer water in the interlayer region. Norrish (1954) had noticed that the crystalline swelling proceeds only to 19 Å. It

is accepted that the coexistence of different hydration states (0W, 1W, 2W) in a smectite sample is common even under controlled conditions. It is also accepted that fractional hydration states correspond to a sample with different integer hydration structures. X–ray diffraction patterns provide evidence that hydration structures evolve gradually from one hydration state to the other through mixed–layer structures composed of discrete hydration states (Ferrage et al., 2005). This could account for experimental data outside of the regions defined by the dotted lines in Figure 5.2(a), which might have been originated from a mixture of montmorillonite at different hydration states.

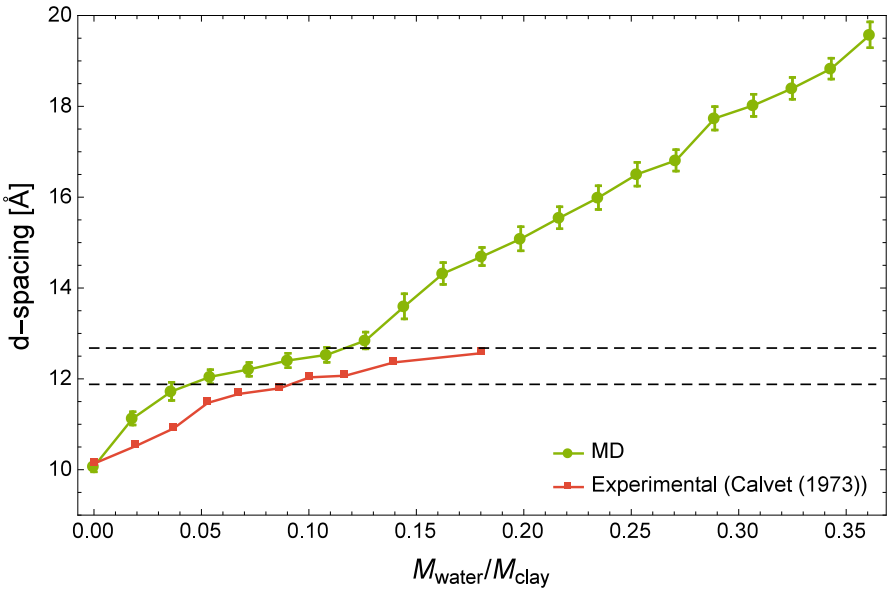
5.2.2 K-montmorillonite

The basal spacing for K-montmorillonite after hydration obtained from the simulations is presented in Figure 5.2(b) along with the experimental data obtained by Calvet (1973). The error bars represent two standard deviations. The results are not consistent with the experiment. However, similar simulations carried out by Suter et al. (2011) present the same behavior, which could demonstrate this deviation is due to the force field itself. It is also possible that the results obtained by Calvet (1973) are subject to careful revision.

Comparing Figure 5.2(a) with 5.2(b), it is possible to see that the basal spacing of dry K-montmorillonite is larger than that of Na-montmorillonite ($\sim$10 Å compared to $\sim$9.4 Å, respectively). A second general difference is that the trend followed by K-montmorillonite evidences only one well–defined expanded structure, that is one water layer between 11.9 Å and 12.7 Å. It does not mean that a second water layer is not formed as water content increases; the change of slope at about 0.16 g H_2O/g clay could be the onset of this second water layer.

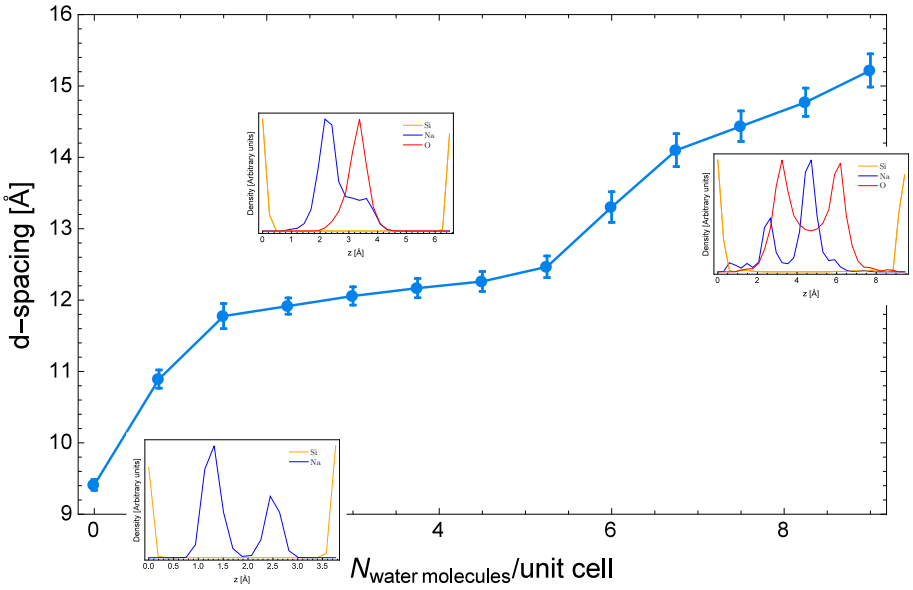


(a) Na-montmorillonite.

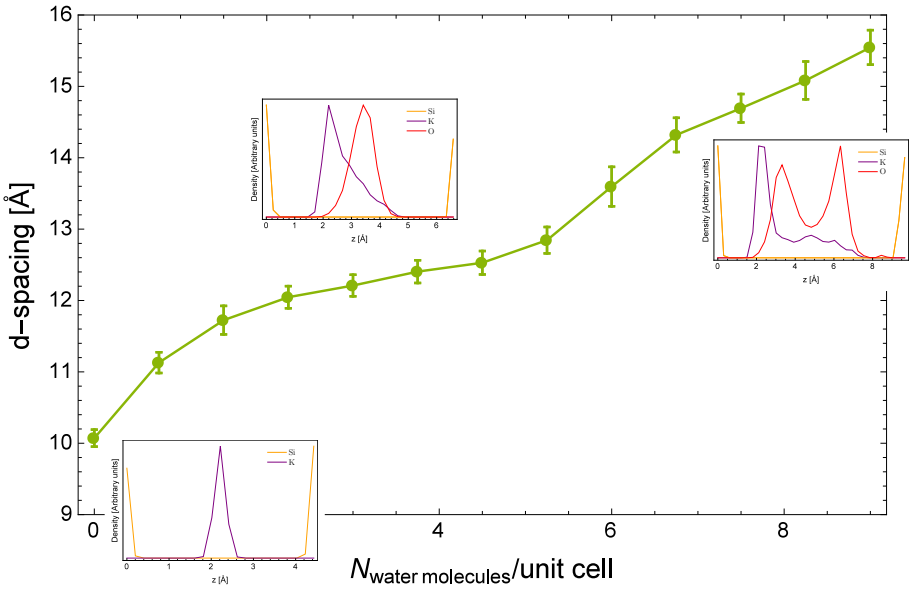


(b) K-montmorillonite.

Figure 5.2: Swelling behavior of montmorillonite clays upon hydration. Comparison of calculated and experimental results.

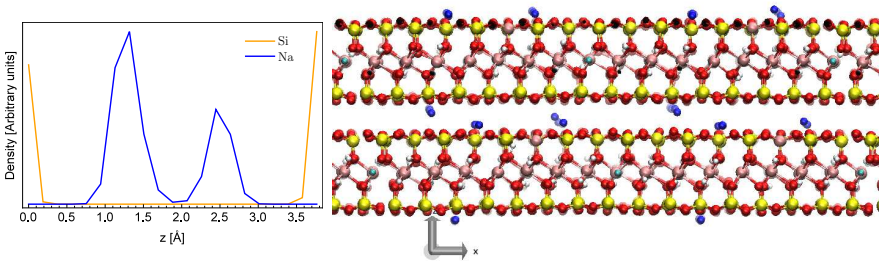


(a) Na-montmorillonite.

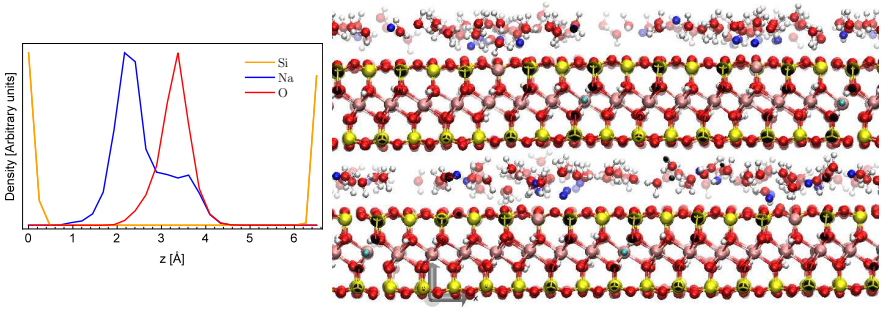


(b) K-montmorillonite.

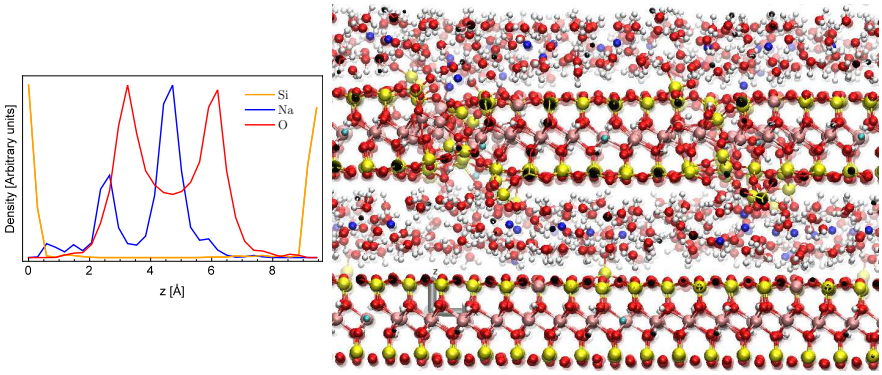
Figure 5.3: Swelling behavior and density profiles for 0W, 1W, and 2W. Color code: ochre – silicon (clay surfaces); red – water oxygen; blue – sodium; magenta – potassium.



(a) Dry montmorillonite. No water laver.

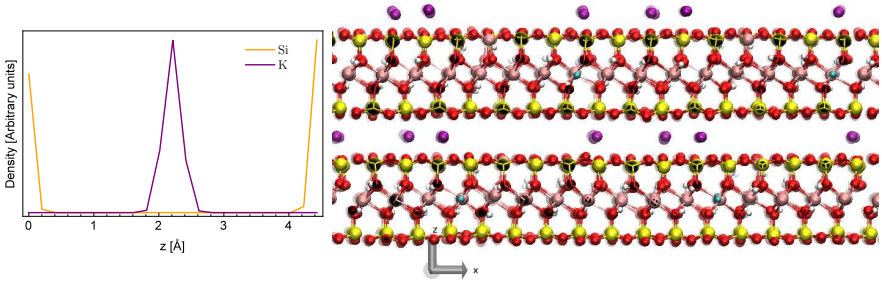


(b) Water monolayer (at a water content of 12 water molecules/4 unit cells).

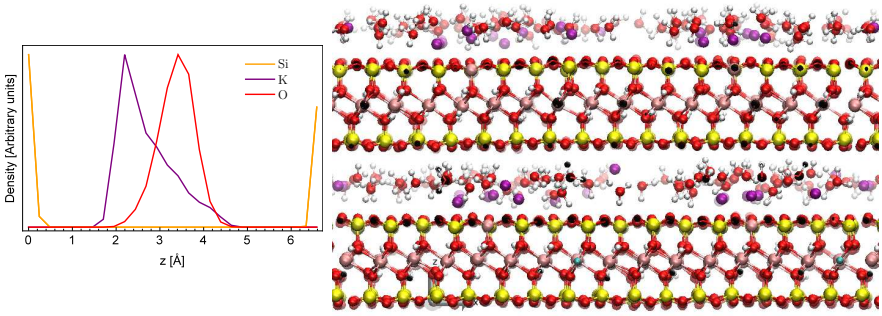


(c) Water bilayer (at a water content of 33 water molecules/4 unit cells).

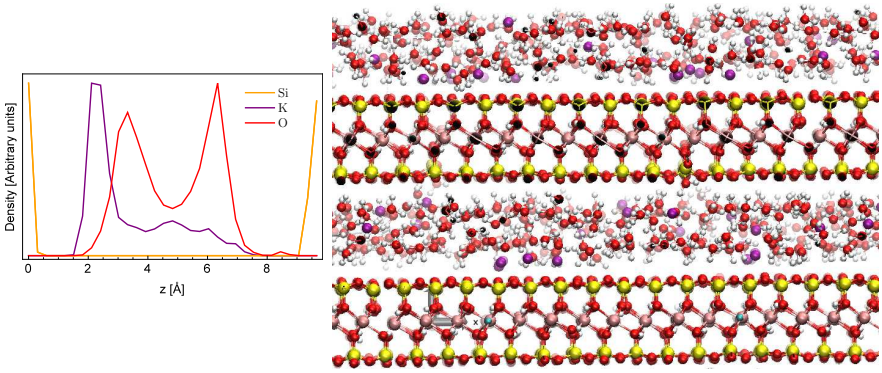
Figure 5.4: Na-montmorillonite. Density profile (left) and interlayer arrangement of cations and O_{water} atoms (right). Color code: yellow – silicon; red – oxygen; pink – aluminum; green – magnesium; white – hydrogen; blue – sodium.



(a) Dry montmorillonite. No water layer.



(b) Water monolayer (at a water content of 12 water molecules/4 unit cells).



(c) Water bilayer (at a water content of 33 water molecules/4 unit cells).

Figure 5.5: K-montmorillonite. Density profile (left) and interlayer arrangement of cations and O_{water} atoms (right). Color code: yellow – silicon; red – oxygen; pink – aluminum; green – magnesium; white – hydrogen; magenta – potassium.

5.3 Distribution of cations and water molecules in the interlayer region

As mentioned in the previous section, water molecules form monolayer and bilayer structures in Na-montmorillonite; the formation of the bilayer structure in K-montmorillonite cannot be noticed readily in Figure 5.2(b). Figure 5.3 shows the average distribution of cations and water molecules[2] in the interlayer region as the basal spacing increases. Particularly, Figure 5.3(b) reveals that in fact a second water layer is formed in the K-montmorillonite, but nonetheless the distribution of cations in the interlayer regions of Na- and K-montmorillonite is quite different.

5.3.1 Na-montmorillonite

Figure 5.4 is a detailed sequence of the accommodation of Na^+ cations and water oxygen atoms in the interlayer region as water content increases and water layers are formed. The ochre curve represents the position of silicon atoms in the clay walls. The wall to the left holds the tetrahedral substitution, the wall to the right presents no substitutions. The charge of the walls is dissimilar and therefore the symmetry is broken, which explains why the density profiles are not symmetrical with respect to the middle plane of the interlayer region. For the dry clay (Figure 5.4(a)), most of the cations are skewed towards the clay surface negatively charged, and some of them are located above the middle plane. With this finding, this computational experiment shows that the cations are attached to the clay surface. Under incremental addition of water molecules the cations relocate until one water layer is formed in the middle plane between clay walls at 9 water molecules/4 unit cells (Figure 5.4(b)). Some of the cations are placed in the same plane as the oxygen

[2]Strictly speaking, the distribution of the oxygen atoms of water molecules.

atoms, but the majority situate between the charged clay wall and the water layer. Further addition of water molecules does not cause the clay structure to expand until after water content reaches 21 water molecules/4 unit cells, meaning that water density increases in the interlayer region and extra water molecules fill void space. This increment of water density, however, does not significantly change the shape of the density profile for Na^+ cations, so that the vast majority still remain skewed towards the charged clay surface. One possible interpretation of this effect is that most of the cations remain attached to the charged surface, probably due to their ionic radius (between 99 pm and 102 pm because these cations are not fully hydrated, see Shannon (1976); Zhou et al. (2002)). They are small enough to fit within the hexagonal structure formed by the tetrahedral arrangement. At this water content, the hydration energy of Na^+ is not large enough to favor its detachment from the clay surface. This interpretation is consistent with the results presented by Emmerich et al. (2015). At 21 water molecules/4 unit cells, an incipient second water layer starts to form. When it is fully formed, at 24 water molecules/4 unit cells, Na^+ cations are partially hydrated and in the same planes as oxygen atoms. As water content increases, the hydration energy of Na^+ cations overcomes the cation–surface attraction energy. More cations detach from the clay surface and occupy the middle region in the interlayer region, in between the two water layers, which results in Na^+ becoming fully hydrated (Figure 5.4(c)). This behavior continues up to 36 water molecules/4 unit cells.

5.3.2 K-montmorillonite

Similarly, Figure 5.5 presents a detailed sequence of the accommodation of K^+ cations and water oxygen atoms in the interlayer region as water content increases and water layers are formed. For the dry clay, all the K^+ cations are located in the

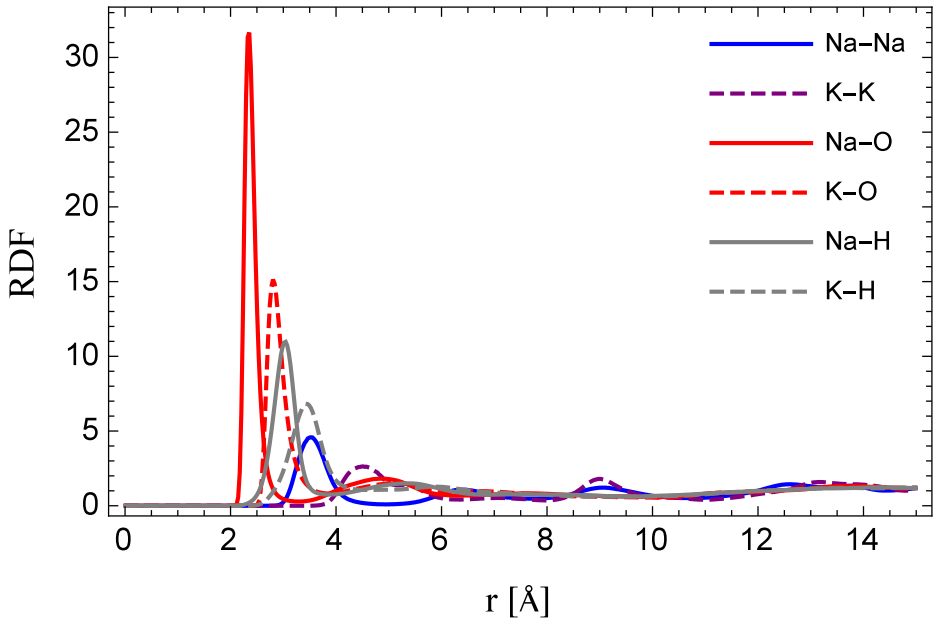
middle plane of the interlayer region with no tendency to skew towards the layer that holds the tetrahedral substitution (Figure 5.5(a)). A plausible explanation is that the ionic radius of K^+, 148 pm (Zhou et al., 2002), is too large to fit within the hexagonal structure formed by the tetrahedral arrangement. It, in turn, would be the reason why dry clay saturated with K^+ cations presents a larger basal spacing than that of dry clay saturated with Na^+ cations. As water content increases, the cations skew towards the wall negatively charged until the first water layer is fully formed at 9 water molecules/4 unit cells (Figure 5.5(b)). A small portion of cations are placed in the same plane as oxygen atoms, but the majority are situated between the clay wall and the water layer. At this point, when the water monolayer is formed, the behavior of Na^+ and K^+ cations is somewhat similar. Further addition of water molecules does not significantly expand the structure until a water content of 15 water molecules/4 unit cell is reached, resulting in the onset of an incipient second water layer. Although this onset point appears earlier for K-montmorillonite, it takes longer to be fully formed, even resulting in water molecules spread in a wider volume in the middle of the interlayer region. At a water content of 27 water molecules/4 unit cells the water layers can be differentiated but a very small amount of K^+ cations are encountered in between the two water layers, which means only a small portion of the cations became hydrated. The majority remain mainly between the clay wall negatively charged and the lower water layer, pushing the walls apart from each other, accounting for the larger swelling effect relative to that of Na-montmorillonite. At this water content, the hydration energy of K^+ cations is not large enough to overcome the cation–surface attraction energy. Further increments of water molecules result in only a small quantity of hydrated cations (Figure 5.5(c)), this behavior being completely different than that of Na^+ cations.

To support the statements made about the differences in cation hydration

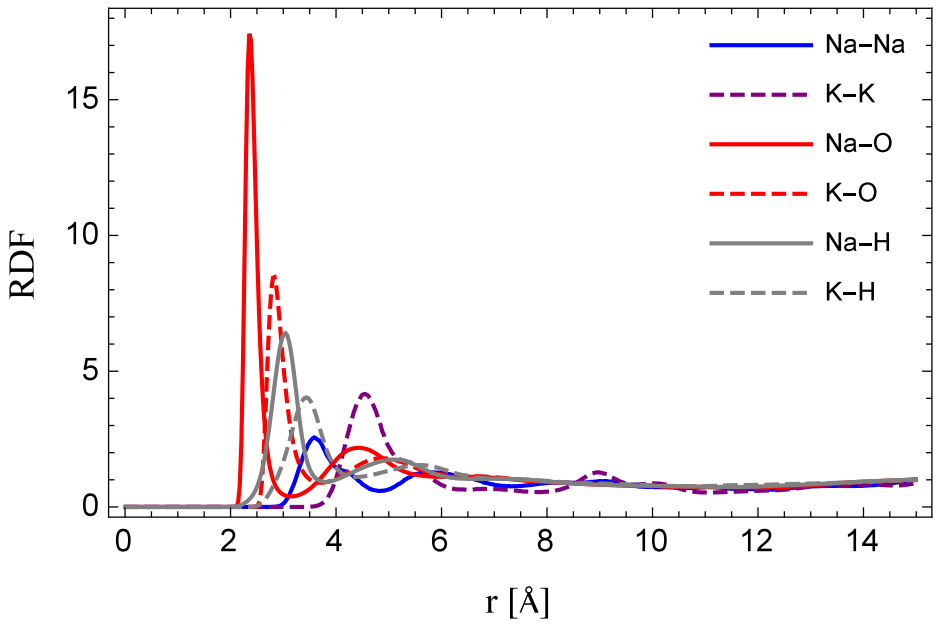
(hydration energy), the radial distribution functions (RDF) for the formation of water monolayer and bilayer were calculated and are presented in Figure 5.6. The RDF provides information about how, on average, the atoms in the system are radially distributed around each other. As a general observation, it can be noted that the smaller the cation, the more pronounced the first cation-O peak, the lower the first trough, and the shorter the peak position, indicating stronger hydration. The cation-H peak position is larger than that of cation-O, which is strong evidence of the hydration structure. These observations are consistent with Zhou et al. (2002). In fact, for the monolayer (Figure 5.6(a)), the first-neighbor peak of Na^+ and K^+ is water molecules, with oxygen atoms facing the cations and hydrogen atoms placed in the opposite direction, which indicates that the cations are surrounded by water molecules with their oxygen atoms (the most electronegative part of the molecule) facing them. In addition to this, the Na^+–O_{water} peak is larger than that of K^+–O_{water}, meaning that the hydration tendency of Na^+ cations is larger than that of K^+ cations. For the bilayer (Figure 5.6(b)), the trends reveal that the first-neighbor peak of both cations is O_{water} and that the Na^+–O_{water} peak is again larger than that of K^+–O_{water}, in accordance with the interpretations made for the monolayer. Interestingly, an observation that deserves further attention is that after the water bilayer is formed, the interaction between K^+ and other K^+ cations is larger than in the case of the monolayer. Thus showing it is easier, for the amount of water present in the interlayer region, to hydrate Na^+ cations than K^+ cations.

5.4 Clay stability and damage

Notice from Figure 5.4(c) that the integrity of the clay structure itself is already compromised at a water content of 33 water molecules/4 unit cells; the arrangement



(a) Formation of water monolayer.



(b) Formation of water bilayer.

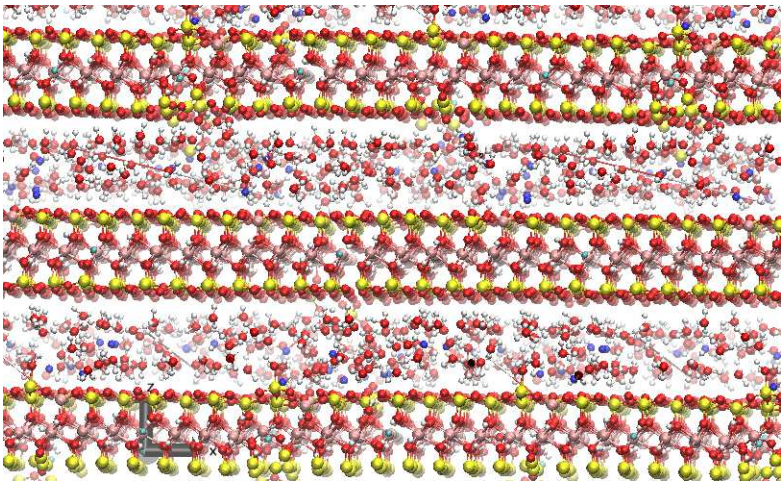
Figure 5.6: Radial distribution functions for cations, oxygen and hydrogen atoms.

of atoms in the walls has begun to distort, although macroscopically it remains stable. As it turns out, further addition of water produces an unstable structure that expands without apparent order. Once the bilayer structure has formed, the vast majority of Na^+ cations are fully hydrated, as discussed in the previous section. The cations are located in the middle plane of the interlayer region, surrounded by water molecules with their oxygen atoms pointing toward the cations, and the hydrogen atoms facing the clay surfaces. The electrostatic interaction between the positive charges (Na^+) and the negative clay surfaces is screened by the water layers, so that hydrogen bonds are now responsible for holding the structure stable. However, hydrogen bonding is not sufficient to accomplish this, so there is no effective coordinate stabilization of the configuration. Cygan et al. (2004) noticed the same effect and proposed that the major contribution to the total energy of the system comes from hydrogen bonding of the large number of the interlayer water molecules such that this region is more representative of bulk water than confined water. Figure 5.7 presents snapshots taken from the simulations for 36 and 39 water molecules/4 unit cells. Figure 5.7(a) reveals that water molecules penetrated the clay layers compromising their structure, and Figure 5.7(b) shows how water molecules invaded the clay layers and detached silicon and oxygen atoms from the tetrahedral layers, which is known as *stability damage*.

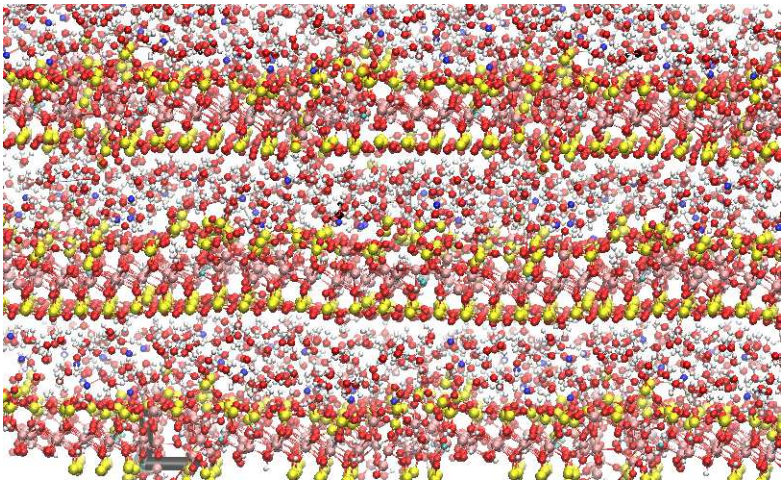
Unlike Na-montmorillonite, K-montmorillonite structure remains stable after insertion of 39 water molecules/4 unit cells, as shown in Figure 5.8(b). The difference with Figure 5.8(a) is evident. In general, water molecules are still positioned at certain distances from the clay walls and only a small portion of the K^+ cations are fully hydrated. As mentioned above, most of the cations remain in between the charged clay surface and the lower water layer, so that the electrostatic interaction between dissimilar charges (cations–positive, clay surfaces–negative) is still consid-

erable, keeping the whole structure stable. In other words, the clay structure fully conserves its integrity. It turns out that this behavior continues until a water content of 45 water molecules/4 unit cells is reached, the moment at which the structure begins to collapse and its integrity is compromised (Figure 5.9(a)). At this point, the hydration energy of the K^+ is large enough to overcome the cation–surface attraction energy. Insertion of three more molecules per four unit cells destroys the structure (Figure 5.9(b)), similar to the situation with 39 water molecules/4 unit cells for Na-montmorillonite. This is a good microscopical picture on how K^+ can prevent clay damage, or at least retard it, as previously noticed by several authors (see for example Boek et al., 1995; Civan, 2007).

It can thus be concluded that stability damage occurs after the cations in the interlayer region become fully hydrated, located at the middle plane, surrounded by water molecules with their oxygen atoms facing the cations while hydrogen atoms face the clay walls. The water layers screen the electrostatic interaction between dissimilar charges. Furthermore, the extra water molecules that do not participate in the hydration of the cations are able to interact with the clay surfaces and diffuse into them, ultimately causing their damage.

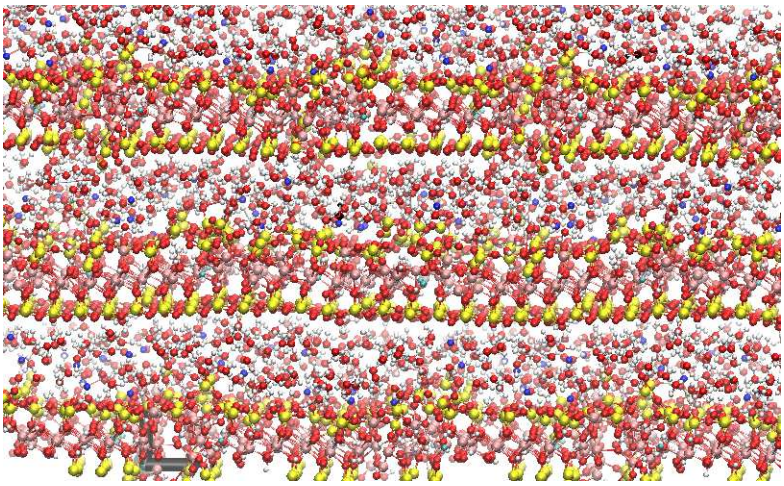


(a) Interlayer region with 36 water molecules/4 unit cells.

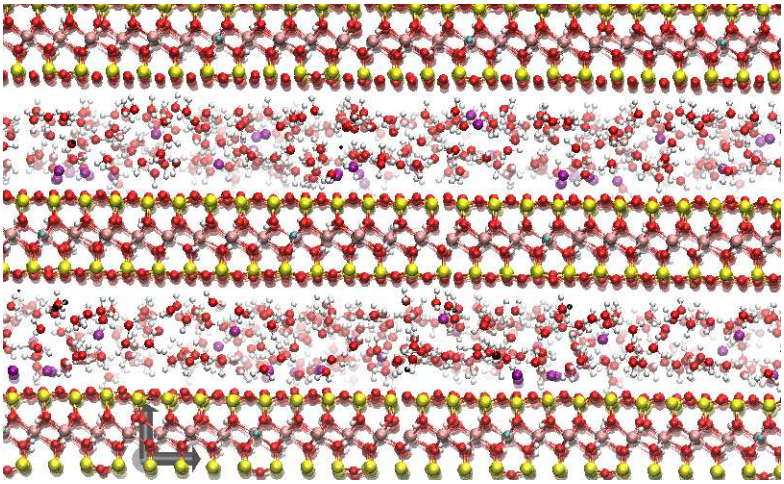


(b) Interlayer region with 39 water molecules/4 unit cells.

Figure 5.7: Snapshot of the Na-montmorillonite looking along the y-axis. Color code: yellow – silicon; red – oxygen; magenta – aluminum; green – magnesium; white – hydrogen; blue – sodium.

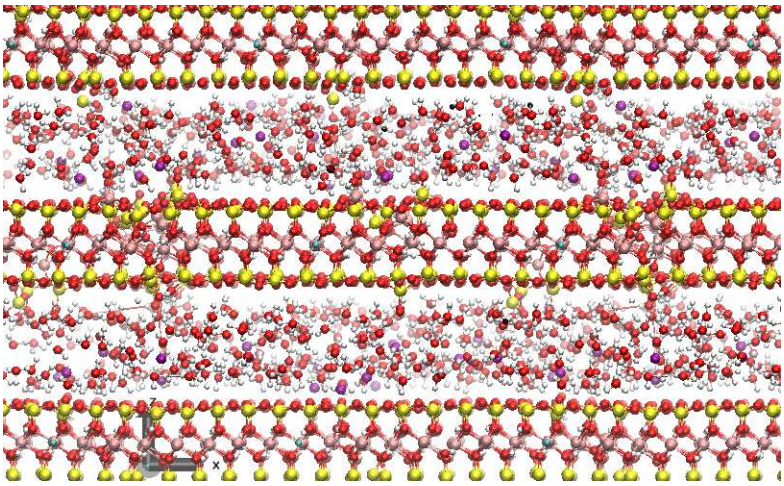


(a) Na-montmorillonite.

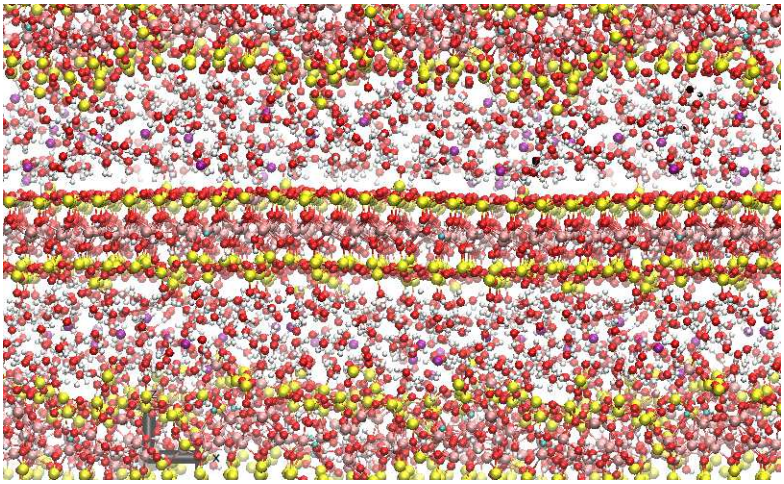


(b) K-montmorillonite.

Figure 5.8: Comparison between interlayer regions with 39 water molecules/4 unit cells. Color code: yellow – silicon; red – oxygen; magenta – aluminum; green – magnesium; white – hydrogen; blue – sodium; magenta – potassium.



(a) Interlayer region with 45 water molecules/4 unit cells.



(b) Interlayer region with 48 water molecules/4 unit cells.

Figure 5.9: Snapshot of the K-montmorillonite looking along the y-axis. Color code: yellow – silicon; red – oxygen; pink – aluminum; green – magnesium; white – hydrogen; magenta – potassium.

Chapter 6

Conclusions and recommendations

6.1 Conclusions

The following conclusions can be drawn from this thesis:

1. The human race has used clays for ages. New frontiers in science and technology have brought about not only new applications and designs but also the need for a better understanding of the behavior of clays. It is not surprising therefore that the study, both theoretical and experimental, of several types of clay has gained the attention of a broad spectrum of the scientific community. This study, nonetheless, is still challenging because smectites are the most heterogeneous class of minerals with a pronounced variety in reactivity. In order to understand how smectites interact with external agents in real systems, it is necessary to first gain insights from theoretical analysis of well–defined structures.

2. Clay damage can have an adverse impact on drilling operations and lead to significantly increased oil and gas well drilling and completion costs. Minimizing the effects of clay swelling is then an important area of study that is

attracting a large amount of attention from both academia and industry. To reduce the impact of clay damage, the underlying mechanisms by which clay minerals swell needs to be revealed so that efficient swelling inhibitors may be designed and developed.

3. Molecular dynamics simulations have proven to be a very powerful tool to investigate microscopic systems for which the complete control of external and internal parameters in experiments at laboratory scales is seemingly impossible. In this particular case, MD simulations were run to investigate the underlying mechanisms by which montmorillonite is damaged. There were identified two main mechanisms: clay swelling and instability of the clay layers.

4. The swelling of clays under contact with water occurs in a stepwise manner, through the formation of one, two, and perhaps three water layers in the interlayer region. Water molecules interact first with such cations, hydrating them, and then the extra water molecules interact with the clay walls.

5. The size and hydration energy of the cations are the factors that condition the arrangement of water molecules and cations in the region between clay sheets. For the dry clay species, the larger ionic radius of K^+, compared to that of Na^+, explains the larger basal spacing of K-montmorillonite compared to that of Na-montmorillonite. The ability of Na^+ cations to bury into the tetrahedral structure explains the higher degree of attachment to the wall compared to that of K^+ cations, whose larger ionic radius prevents them from burying and attaching to the clay surface. Under contact with water molecules, the higher hydration tendency of Na^+ cations explains why it is easier for water to detach and hydrate Na^+ cations while they move and occupy the middle plane of the interlayer region.

6. Stability damage of clays occurs after the cations in the interlayer region are fully hydrated, located at the middle plane, surrounded by water molecules with their oxygen atoms facing the cations while hydrogen atoms face the clay walls. The water layers screen the electrostatic interaction between dissimilar charges. The extra water molecules that do not participate in the hydration of the cations are able to interact with the clay surfaces, diffuse into them, and ultimately cause their damage.

6.2 Recommendations

For future work, the author recommends:

1. Running new simulations to consider other factors that might have a large impact in the swelling of clays, such as the charge of the balancing cations (for example, to compare with the results obtained for Ca-montmorillonite, whose countercation is Ca^{2+}), external pressure and temperature (in the range of relevance for oil and gas bearing formations).

2. Including other molecules of interest in petroleum engineering that are compatible with the Clayff force field. For example, carbon dioxide (CO_2) in enhanced oil recovery; polymers with low molecular weight (polyethylene glycols –PGEs– and polypropylene glycols –PPGs) and high molecular weight (partially hydrolyzed polyacrylamide –PHPA) in designing drilling fluids and polymer waterflooding; and low salinity water injection in formation damage. The spectrum of applications is potentially quite large.

3. Considering other study areas of clays, of interest in petroleum engineering, using molecular dynamics simulations. Adsorption of water molecules by montmorillonites is accompanied by a large increase in the basal layer spacing. This

swelling process significantly impacts the structural and mechanical properties of clays. Determining the elastic properties of clays at reservoir conditions could is a topic with potential applications in borehole stability and hydraulic fracturing.

References

Accelyrs, Inc. (2014). *Materials Studio Software*. Accelyrs, Inc. San Diego, CA.

Allen, M. and D. Tildesley (1989). *Computer Simulation of Liquids*. Oxford Science Publ. Clarendon Press. New York, NY, USA.

Amaefule, J., D. Kersey, D. Norman, and P. Shannon (1988). Advances in formation damage assessment and control strategies. In *Annual Technical Meeting*. Petroleum Society of Canada. Calgary, Alberta.

Anderson, R., H. Greenwell, J. Suter, R. Jarvis, and P. Coveney (2010). Towards the design of new and improved drilling fluid additives using molecular dynamics simulations. *Anais da Academia Brasileira de Ciências 82*(1), 43–60.

Anderson, R., I. Ratcliffe, H. Greenwell, P. Williams, S. Cliffe, and P. Coveney (2010). Clay swelling – A challenge in the oilfield. *Earth-Science Reviews 98*, 201–216.

Anthony, J., R. Bideaux, K. Bladh, and M. Nichols (Eds.) (2001). *Handbook of Mineralogy*. Mineralogical Society of America. Online version on http://www.handbookofmineralogy.org. Accesed on May 19th, 2015.

Barshad, I. (1952). Factors affecting the interlayer expansion of vermiculite and

montmorillonite with organic substances. *Soil Science Society of America Journal 16*(2), 176–182.

Bennion, B. (2002). An overview of formation damage mechanisms causing a reduction in the productivity and injectivity of oil and gas producing formations. *Journal of Canadian Petroleum Technology 41*(11), 29–36.

Berendsen, H., J. Postma, W. van Gunsteren, and J. Hermans (1981). *Intermolecular Forces: Proceedings of the Fourteenth Jerusalem Symposium on Quantum Chemistry and Biochemistry Held in Jerusalem, Israel, April 13–16, 1981*, Chapter Interaction models for water in relation to protein hydration, pp. 331–342. Springer Netherlands. Dordrecht.

Bishop, S. (1997). The experimental investigation of formation damage due to the induced flocculation of clays within a sandstone pore structure by a high salinity brine. SPE 38156 paper, presented at the 1997 SPE European Formation Damage Conference held in The Hague, The Netherlands, 2–3 June.

Bloys, B., N. Davis, B. Smolen, L. Bailey, L. Fraser, and M. Hodder (1994). Designing and managing drilling fluid. *Schlumberger Oilfield Review 6*, 33–43.

Boek, E., P. Coveney, and N. Skipper (1995). Monte Carlo molecular modeling studies of hydrated Li-, Na-, and K-smectites: Understanding the role of potassium as a clay swelling inhibitor. *J. Am. Chem. Soc. 117*(50), 12608–12617.

Bordallo, H., L. Aldridge, G. Churchman, W. Gates, M. Telling, K. Kiefer, P. Fouquet, T. Seydel, and S. Kimber (2008). Quasi-elastic neutron scattering studies on clay interlayer–space highlighting the effect of the cation in confined water dynamics. *J. Phys. Chem. C 112*(36), 13982–13991.

Born, M. and R. Oppenheimer (1927). Zur quantentheorie der molekeln. *Annalen der Physik 389*(20), 457–484.

Boulet, P., H. Greenwell, S. Stackhouse, and P. Coveney (2006). Recent advances in understanding the structure and reactivity of clays using electronic structure calculations. *Journal of Molecular Structure*, 33–48. THEOCHEM 762.

Bransden, B. and C. Joachain (1983). *Physics of Atoms and Molecules*. Longman Scientific & Technical. Copublished in the United States with John Wiley & Sons, Inc. New York.

Brindley, G. and R. Wardle (1970). Monoclinic and triclinic forms of pyrophyllite and pyrophyllite anhydride. *American Mineralogist 55*, 1259–1272.

Bucke, Jr., D. and C. Mankin (1971). Clay-mineral diagenesis within interlaminated shales and sandstones. *Journal of Sedimentary Petrology 41*(4), 971–981.

Calvet, R. (1973). Hydration of montmorillonite and diffusion of exchangeable cations. 1. Hydration of montmorillonite saturated by monovalent cations. *Annales Agronomiques 24*(1), 77–133.

Campos, D. *Fundamentos de Física Atómica y Molecular*. Editorial Universidad Nacional. Bogota, Colombia.

Chou Chang, F., N. Skipper, and G. Sposito (1995). Computer simulation of interlayer molecular structure in sodium montmorillonite hydrates. *Langmuir 11*(7), 2734–2741.

Civan, F. (2007). *Reservoir Formation Damage. Fundamentals, Modeling, Assessment, and Mitigation* (Second ed.). Gulf Professional Publishing. Burlington, MA 01803, USA.

Cygan, R., J. Liang, and A. Kalinichev (2004). Molecular models for hydroxide, oxhyhydroxide, and clay phases and the development of a general force field. *J. Phys. Chem. B 108*(4), 1255–1266.

Cygan, R., V. Romanov, and E. Myshakin (2012). Molecular simulation of carbon dioxide capture by montmorillonite using an accurate and flexible force field. *J. Phys. Chem. C 116*, 13079–13091.

da Silva, G., J. Fossum, E. DiMasi, K. Måløy, and S. Lutnæs (2002). Synchroton x–ray scattering studies of water intercalation in a layered synthetic silicate. *Phys. Rev. E 66*, 011303.

Emmerich, K., F. Koeniger, H. Kaden, and P. Thissen (2015). Microscopic structure and properties of discrete water layer in Na-exchanged montmorillonite. *Journal of Colloid and Interface Science 448*, 24–31.

Emmerich, K., F. Wolters, G. Kahr, and G. Lagaly (2009). Clay profiling: The classification of montmorillonites. *Clays and Clay Minerals 57*(1), 104–114.

Ferrage, E., B. Larson, B. Sakharov, and V. Drits (2005). Investigtion of smectite hydration properties by modeling experimental X-ray diffraction patterns: Part I, Montmorillonite hydration properties. *American Mineralogist 90*, 1358–1374.

Fu, M., Z. Zhang, and P. Low (1990). Changes in the properties of a montmorillonite–water system during the adsorption and desorption of water: hysteresis. *Clays and Clay Minerals 38*(5), 485–492.

Gale, J. and A. Rohl (2003). The General Utility Lattice Program (GULP). *Molecular Simulation 29*(5), 291–341.

Giesting, P., S. Guggenheim, A. Koster van Gross, and A. Busch (2012). Interaction of carbon dioxide with Na-exchanged montmorillonite at pressures to 640 bar:

Implications for CO_2 sequestration. *International Journal of Greenhouse Gas Control 8*, 73–81.

Gray, G. and H. Darley. *Composition and Properties of Oil Well Drilling Fluids*. Gulf Publishing Company. Houston, TX.

Gruner, J. (1934). The crystal structures of talc and pyrophyllite. *Zeitschrift für Kristallographie, Kristallgeometrie, Kristallphysic, Kristallchemie 88*, 412–419.

Halgren, T. (1992). Representation of van der Waals (vdW) interactions in molecular mechanics force fields: potential form, combination rules, and vdW parameters. *J. Am. Chem. Soc. 114* (20), 7827–7843.

Humphrey, W., A. Dalke, and K. Schulten (1996). VMD: Visual molecular dynamics. *Journal of Molecular Graphics 14* (1), 36–38.

Ilton, E., H. Schaef, O. Qafoku, K. Rosso, and A. Felmy (2012). In situ X-ray diffraction study of Na^+ saturated montmorillonite exposed to variably wet super critical CO_2. *Environmental Science & Technology 46*, 4241–4248.

Landau, L. and E. Lifshitz (1977). *Course of Theoretical Physics* (Third ed.), Volume 3: Quantum Mechanics – Non-relativistic Theory. Pergamon Press. Exeter, Great Britain.

Lauterwasser, C. (2005). Small sizes that matter: Opportunities and risks of nanotechnologies. Technical report, Allianz Center for Technology. Report in cooperation with the OECD International Futures Program.

Lee, J. and S. Guggenheim (1981). Single crystal X-ray refinement of pyrophyllite–$1Tc$. *American Mineralogist 66*, 350–357.

Martínez, L., R. Andrade, E. Birgin, and J. Martínez (2009). Packmol: A package for building initial configurations for molecular dynamics simulations. *J. Comp. Chem. 13*(30), 2157–2164.

McCabe, R. (1996). Clay Chemistry. In D. Bruce and D. O'Hare (Eds.), *Inorganic Materials* (Second ed.)., Chapter 5, pp. 313–376. John Wiley and Sons. New York.

Mignon, P., P. Ugliengo, M. Sodupe, and E. Hernandez (2010). Ab initio molecular dynamics study of the hydration of Li^+, Na^+ and K^+ in a montmorillonite model. influence of isomorphic substitution. *Phys. Chem. Chem. Phys. 12*, 688–897.

Minisini, B. and F. Tsobnang (2005). Ab initio comparative study of montmorillonite structural models. *Applied Surface Science 242*, 21–28.

Mondshine, T. (1973). A new potassium based mud system. SPE 4516 paper, presented at the 48th Annual Fall Meeting of the Society of Petroleum Engineers of AIME, held in Las Vegas, Nevada, September 30–October 3.

Mungan, N. (1989). Discussion of An overview of formation damage. *Journal of Petroleum Technology 41*(11), 1224.

Myshakin, E., W. Saidi, V. Romanov, R. Cygan, and K. Jordan (2013). Molecular dynamics simulations of carbon dioxide intercalation in hydrated Na–montmorillonite. *J. Phys. Chem. C 117*, 11028–11039.

Nelson, S. (2014). Mineralogy. Lecture notes. Tulane University, Department of Earth and Environmental Sciences.

Norrish, K. (1954). The swelling of montmorillonite. *Discussions of the Faraday Society 18*, 120–134.

Nosé, S. (1984a). A molecular dynamics method for simulations in the canonical ensemble. *Mol. Phys. 52*(2), 255–268.

Nosé, S. (1984b). A unified formulation of the constant temperature molecular dynamics methods. *J. Chem. Phys. 81*(1), 511–519.

Nosé, S. (1991). Constant temperature molecular dynamics methods. *Prog. Theor. Phys. Suppl. 103*, 1–46.

Ohen, H. and F. Civan (1993). Simulation of formation damage in petroleum reservoirs. *SPE Advanced Technology Series 1*(1), 27–35.

Parrinello, M. and A. Rahman (1981). Polymorphic transitions in single crystals: A new molecular dynamics method. *J. Appl. Phys. 52*(12), 7182–7190.

Plimpton, S. (1995). Fast parallel algorithms for short–range molecular dynamics. *J. Comp. Phys. 117*, 1–19.

Rayner, J. and G. Brown (1964). Structure of pyrophyllite. In W. Bradley and S. Bailey (Eds.), *Thirteenth National Conference on Clays and Clay Minerals*, pp. 73–84.

Reed, M. (1977). Formation permeability damage by mica alteration and carbonate dissolution. *Journal of Petroleum Technology 29*(9), 1056–1060.

Schoonheydt, R. and C. Johnston (2013). Surface and Interface Chemistry of Clay Minerals. In F. Bergaya and G. Lagaly (Eds.), *Handbook of Clay Science, Developments in Clay Science*, Volume 5, Chapter 5, pp. 139–172. Elsevier.

Shannon, R. (1976). Revised effective ionic radii and systematic studies of interatomic distances in halides and chalcogenides. *Acta Cryst. A32*, 751–767.

Sun, L., J. Tanskanen, J. Hirvi, S. Kasa, T. Schatz, and T. Pakkanen (2015). Molecular dynamics study of montmorillonite crystalline swelling: roles of interlayer cation species and water content. *Chemical Physics 455*, 23–31.

Suter, J., P. Coveney, R. Anderson, H. Greenwell, and S. Cliffe (2011). Rule based design of clay–swelling inhibitors. *Energy Environ. Sci. 4*, 4572–4586.

Teleman, O., B. Jönsson, and S. Engström (1987). A molecular dynamics simulation of a water model with intramolecular degrees of freedom. *Molecular Physics 60*(1), 193–203.

Tsipursky, S. and V. Drits (1984). The distribution of octahedral cations in the 2:1 layers of dioctahedral smectites studied by oblique–texture electron diffraction. *Clay Minerals 19*, 177–193.

Uddin, F. (2008). Clays, nanoclays, and montmorillonite minerals. *Metallurgical and Materials Transactions A 39A*, 2804–2814.

Wardle, R. and G. Brindley (1972). The crystal structures of pyrophyllite, $1Tc$, and of its dehydroxylate. *American Mineralogist 57*, 732–750.

Zheng, Y., A. Zaoui, and I. Shahrour (2011). A theoretical study of swelling and shrinking of hydrated Wyoming montmorillonite. *Applied Clay Science 51*, 177–181.

Zhou, J., X. Lu, Y. Wang, and J. Shi (2002). Molecular dynamics study on ionic hydration. *Fluid Phase Equilibria 194-197*, 257–270.

Zvyagin, B., K. Mishchenko, and S. Soboleva (1969). Structure of pyrophyllite and talc in relation to the polytypes of mica–type minerals. *Soviet Physics Crystallography 13*, 511–515.